nature communications

Article

https://doi.org/10.1038/s41467-025-58778-3

AAV vectors trigger DNA damage response-dependent pro-inflammatory signalling in human iPSC-derived CNS models and mouse brain

Received: 26 March 2024

Accepted: 1 April 2025

Published online: 18 April 2025

Check for updates

Helena Costa-Verdera[1,2], Vasco Meneghini[1,3], Zachary Fitzpatrick[2], Monah Abou Alezz[1], Emily Fabyanic[2], Xin Huang[2], Yulia Dzhashiashvili[2], Avantika Ahiya[2], Elisabeth Mangiameli[1], Erika Valeri[1], Giovanni Crivicich[1,3], Silvia Piccolo[1], Ivan Cuccovillo[1], Roberta Caccia[1], Ying Kai Chan[4,8], Bérangère Bertin[5,6], Giuseppe Ronzitti[5,6], Esteban A. Engel[2], Ivan Merelli[1], Federico Mingozzi[2], Angela Gritti[1,3], Klaudia Kuranda[2] & Anna Kajaste-Rudnitski[1,7]

Adeno-associated viral (AAV) vector-based gene therapy is gaining foothold as treatment for genetic neurological diseases with encouraging clinical results. Nonetheless, dose-dependent adverse events have emerged in recent clinical trials through mechanisms that remain unclear. We have modelled here the impact of AAV transduction in cell models of the human central nervous system (CNS), taking advantage of induced pluripotent stem cells. Our work uncovers vector-induced innate immune mechanisms that contribute to cell death. While empty AAV capsids were well tolerated, the AAV genome triggered p53-dependent DNA damage responses across CNS cell types followed by the induction of inflammatory responses. In addition, transgene expression led to MAVS-dependent activation of type I interferon responses. Formation of DNA damage foci in neurons and gliosis were confirmed in murine striatum upon intraparenchymal AAV injection. Transduction-induced cell death and gliosis could be prevented by inhibiting p53 or by acting downstream on STING- or IL-1R-mediated responses. Together, our work identifies innate immune mechanisms of vector sensing in the CNS that can potentially contribute to AAV-associated neurotoxicity.

Gene therapy with adeno-associated viral (AAV) vectors has become a promising treatment option for genetic neurodegenerative and neuromuscular diseases for which there is currently no cure. Nonetheless, bypassing the blood-brain barrier, achieving broad central nervous system (CNS) transduction and rescuing all affected areas remains a challenge that requires the administration of high AAV vector doses in vivo either systemically or locally, with the risk of inducing cytotoxic immune reactions[1–3]. Moreover, at these high doses, intravenous AAV

[1]San Raffaele Telethon Institute for Gene Therapy, IRCCS San Raffaele Scientific Institute, Milan, Italy. [2]Spark Therapeutics, Inc., Philadelphia, PA, USA. [3]Vita-Salute San Raffaele University, Milan, Italy. [4]Wyss Institute for Biologically Inspired Engineering, Harvard University, Boston, MA, USA. [5]Genethon, Evry, France. [6]Université Paris-Saclay, University Evry, Inserm, Genethon, Integrare Research Unit UMR_S951, Evry, France. [7]Department of Biology and Biotechnology, University of Pavia, Pavia, Italy. [8]Present address: Cirrus Therapeutics, Cambridge, MA, USA. e-mail: anna.kajaste@unipv.it

vector administration has been associated with some cases of systemic adverse events and lethality recently reported in clinical trials of X-linked myotubular myopathy (MTM)[4] and Duchenne muscular dystrophy (DMD)[5], often due to toxicity in off-target organs such as the liver or to thrombotic microangiopathy, highlighting the importance of improving safety and efficacy of this technology.

AAV-mediated CNS gene delivery has shown overall clinical safety and efficacy in a number of clinical trials[6]. However, studies in non-human primates (NHPs) and clinical trials have revealed that both local and systemic treatment with AAV vectors can induce dose-dependent toxicities in the central[7–13] and peripheral[14,15] nervous systems, characterized by neuronal loss in the brain parenchyma or in the dorsal root ganglia (DRG), respectively. Neurological signs have also been reported following direct AAV injection into the brain in a clinical trial for late infantile Batten disease[16]. Although in some cases the observed toxicity was attributed to the packaging of toxic payload and could be prevented by improving the manufacturing process[7], in most studies the causes leading to toxicity remain unclear, highlighting the need to better understand the mechanisms underlying the occurrence of such neurological signs.

Because of the limited accessibility and the challenges of monitoring immune responses in the nervous tissue in patients, mostly limited to magnetic resonance imaging (MRI), it is difficult to study and predict immune responses and toxicity caused by AAV transduction in this tissue, especially when symptoms are not clinically evident. Of note, existing reports in NHPs show no evidence of cytotoxic T cell responses typically observed upon liver or muscle gene transfer[14]. Consequently, the FDA has endorsed efforts to identify the causes of AAV-mediated neurotoxicity and develop strategies to monitor and mitigate them.

Most existing research addressing AAV-associated adverse events has centred on adaptive immune responses triggered by the vector capsid[2,17], the role of capsid and genome sensing by toll-like receptors (TLRs) on peripheral innate immune cells in the induction of adaptive immunity[18–22], as well as on humoral and complement responses[23–25]. However, the impact of AAV transduction on target-cell intrinsic innate immune mechanisms, such as nucleic acid sensing in cell toxicity and tissue inflammation, remain largely unknown. Links between target-cell toxicity and intrinsic innate sensing have been reported in the context of ex vivo gene transfer with AAV vectors[26]. Importantly, cell-intrinsic antiviral mechanisms can contribute to the establishment of inflammation, cause host-cell toxicity and/or limit viral vector transduction[27]. We and others have previously shown that AAV vectors can induce DNA-damage responses (DDR) in cells such as hematopoietic stem and progenitor cells (HSPCs), compromising the transduction efficacy, viability and engraftment capacity of these cells in vivo[26,28]. Yet, the impact of DDR and innate signalling on the safety and efficacy of AAV-mediated in vivo gene transfer remains to be addressed.

Antiviral defences are species- and cell-type dependent, with neurons harbouring specific immune mechanisms[29,30], and the signalling pathways activated by viral vectors in HSPCs differ between human and murine cells[26]. Similarly, the tissue tropism and transduction efficacy of different AAV serotypes varies across species[31,32]. To address the mechanisms leading to AAV-mediated neurotoxicity in relevant human CNS cell types, we have investigated here the impact of AAV transduction on cell-autonomous signalling and innate immunity in different neural cell types, taking advantage of human induced pluripotent stem cell (hiPSC)-based technologies. Bulk and single-cell transcriptomics together with functional assays revealed early induction of p53-dependent DDR and cell death signatures by the AAV genome followed by transgene expression-dependent pro-inflammatory and type I interferon (IFN) signalling in hiPSC-derived neurons and glial cells, in 2D cultures and 3D brain spheroids. Similar DDR activation and pro-inflammatory responses were confirmed in vivo in mice upon intraparenchymal (IPa) injection with AAV9, a clinically relevant serotype to target the CNS. Transduction-related neuron toxicity could be curbed by preventing STING or IL-1R signalling downstream of p53, whereas type I IFN signalling seemed to be dependent on Mitochondrial Antiviral Signalling (MAVS) sensor. Finally, proof-of-concept experiments suggest that p53 and STING inhibition can modulate astrocyte activation in vivo and in vitro. Together, these findings open new avenues for the development of safer CNS-directed AAV gene therapies, if confirmed by future clinical investigations.

Results

AAV transduction triggers DNA damage responses and cell death in hiPSC-derived neurons and astrocytes

To compare simultaneously the transduction efficacy and the signalling induced by different AAV serotypes in cells of the CNS in a human context, we first transduced highly enriched 2D cultures of hiPSC-derived neurons or astrocytes, respectively (Fig. S1). hiPSC-derived neurons and astrocytes were transduced side-by-side with AAV vectors of different serotypes, encoding for green fluorescent protein (GFP) under the control of the CAG promoter. Cells were collected after 48 h for the assessment of vector-triggered signalling pathways by bulk RNA sequencing (RNAseq) (Fig. 1). The serotypes and MOI used for each vector and cell type are detailed in Supplementary Table 1.

A link between transduction efficiency and the magnitude of the induced signalling was observed in both cell types, with AAV2 and AAV6 showing the highest transduction levels as measured by flow cytometry (Fig. 1A, S2A) as well as vector genome copies (Fig. 1B), together with the highest level of transcriptional changes induced (Figs. 1C, D; S3, S4). Higher tropism of AAV2 and AAV6 was also confirmed in primary human neuron cultures (Fig. S2B). At the pathway level, top induced genes were associated with p53 activation, TNFα signalling via NF-κB and inflammatory responses, for both hiPSC-derived neurons and astrocytes (Fig. 1E, F), whereas downregulated genes were mostly involved in cell division, consistent with the activation of p53 and indicative of a DNA-damage response. Top upregulated genes included p53-dependent genes (CDKN1A/P21, PHLDA3, GDF15), pro-apoptotic genes (FAS, BAX, TNFRSF10 superfamily death receptors) as well as pro-inflammatory cytokines and chemokines (IL1R, IL1A/B, CXCL8) (Fig. 1G, H). Of note, empty AAV9 capsid purified as previously described[33] did not induce any significant transcriptional changes compared to untransduced controls, in contrast to the full AAV9 vector (Fig. 1E–H, Fig. S3A, S4A), suggesting that the vector genome is required for the detected signalling. The same was confirmed for empty AAV2 in hiPSC-derived astrocytes in terms of upregulation of selected genes (P21, CXCL8, IL1B), chosen as representative from Fig. 1H (Fig. S5).

Given the clinical relevance of AAV9 in CNS-targeting gene therapies and its involvement in reported brain and DRG toxicities, we further investigated the induction of functional markers of DNA-damage responses and potential vector-related neurotoxicity in hiPSC-derived neurons transduced for 48 h with full or empty AAV9 (Fig. 2). A significant increase in the phosphorylated form of histone γH2AX (p-γH2AX), responsible for recruiting DNA repair proteins to the damage site, and the cleaved form of caspase 3 (cC3), a cell death marker, were recorded in hiPSC-derived neurons transduced with full, but not with empty AAV9 (Fig. 2A–C). Similar induction of vector-triggered toxicity markers was observed in hiPSC-derived astrocytes (Fig. S6). Together, these results indicate that AAV transduction triggers DNA damage signalling and consequent toxicity in a vector genome-dependent manner in hiPSC-derived neural cells.

Single-cell transcriptomics reveal early p53 activation followed by inflammation and interferon signalling in mixed 2D cultures and 3D brain spheroids

To assess the signalling induced by AAV in a more complex microenvironment, we used AAV9 to transduce hiPSC-derived mixed 2D

https://doi.org/10.1038/s41467-025-58778-3

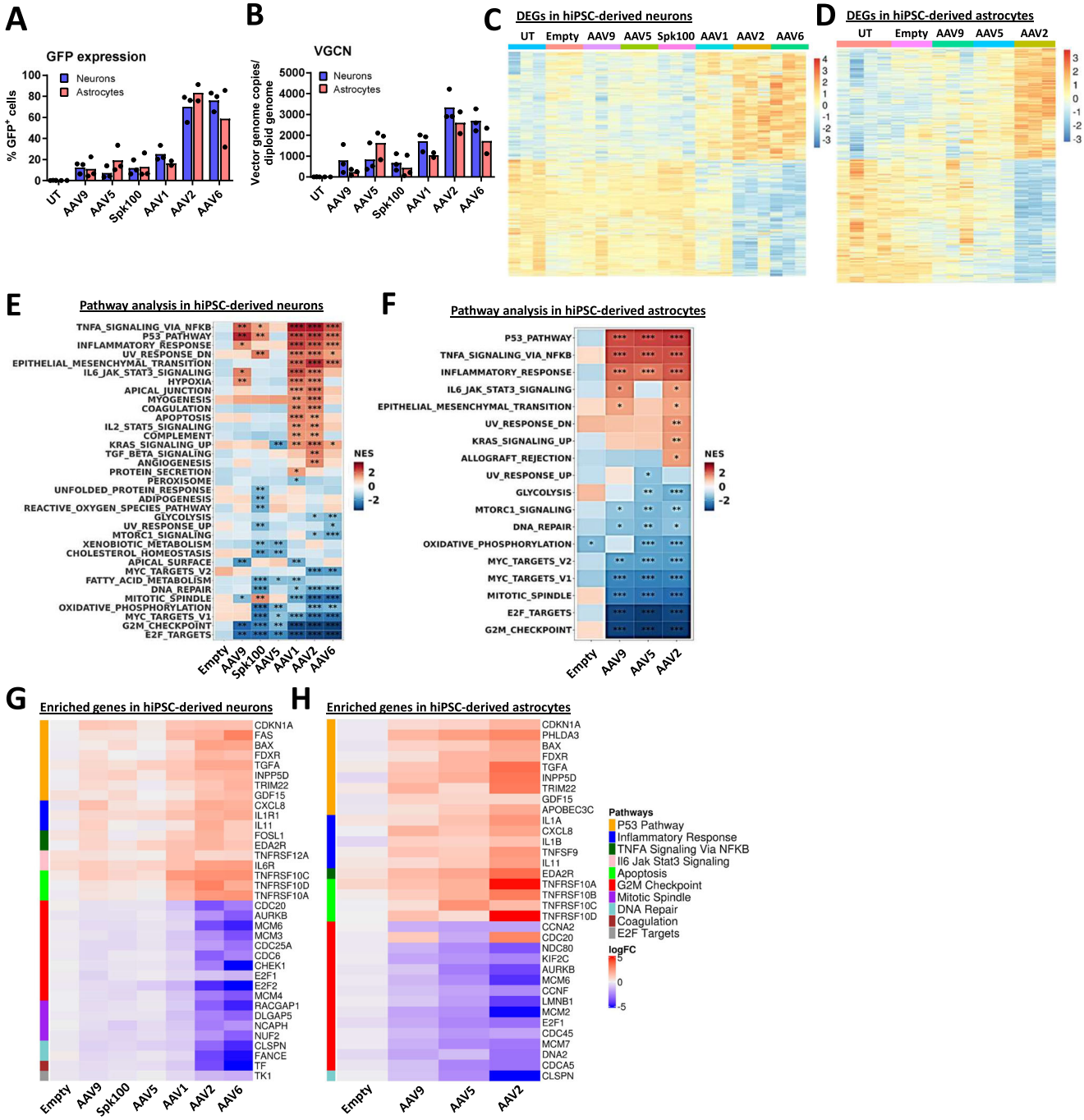

Fig. 1 | AAV vectors elicit transduction-dependent transcriptional alterations in hiPSC-derived neurons and astrocytes. Quantification of vector transduction efficiency by FACS analysis of GFP expression (**A**) and genome copy numbers (**B**) on hiPSC-derived neurons and astrocytes harvested 48 h post-transduction. Data are shown as mean between independent experiments ($n = 3$ for neurons, $n = 3$ for astrocytes transduced with AAV9, AAV5, Spk100 and UT; $n = 2$ for astrocytes transduced with AAV1, AAV2 and AAV6). **C**, **D** Heatmaps representing the level of differentially expressed genes (DEGs) in fold compared to untransduced (UT) samples. Each column constitutes one biological replicate. Heatmaps showing the enriched GSEA terms in hiPSC-derived neurons (**E**) and astrocytes (**F**) against the Hallmark gene set (Molecular Signatures Database). Each column represents the average between $n = 3$ biological replicates for all conditions except astrocytes UT ($n = 4$). GSEA was performed on logFC fold changes in gene expression in transduced samples compared to UT controls using Kolmogorov-Smirnov test with FDR for multiple test correction (NES, normalized enrichment score; *, adjusted $P < 0.05$; **, adjusted $P < 0.01$; ***, adjusted $P < 0.01$). Heatmaps showing the top upregulated and downregulated genes in hiPSC-derived neurons (**G**) and astrocytes (**H**) and the pathways they are associated with according to the Hallmark gene set. Source data are provided as a Source Data file.

cultures (Fig. 3A) composed of neurons, astrocytes and oligodendrocytes at different stages of maturation, as confirmed by single-cell RNAseq (scRNAseq) analysis (Figs. 3B, C, S7). Analysis of GFP mRNA distribution by scRNAseq showed higher AAV9-mediated GFP expression by astrocytes and oligodendrocytes as compared to neurons, suggesting a higher tropism for these cell types in the in vitro setting (Fig. 3D). Analysis of signalling pathways at days two and four post-transduction showed a cell and time-dependent response. Astrocytes and oligodendrocytes were the most responsive to the vector, possibly due to the higher transduction rates and to their role

https://doi.org/10.1038/s41467-025-58778-3

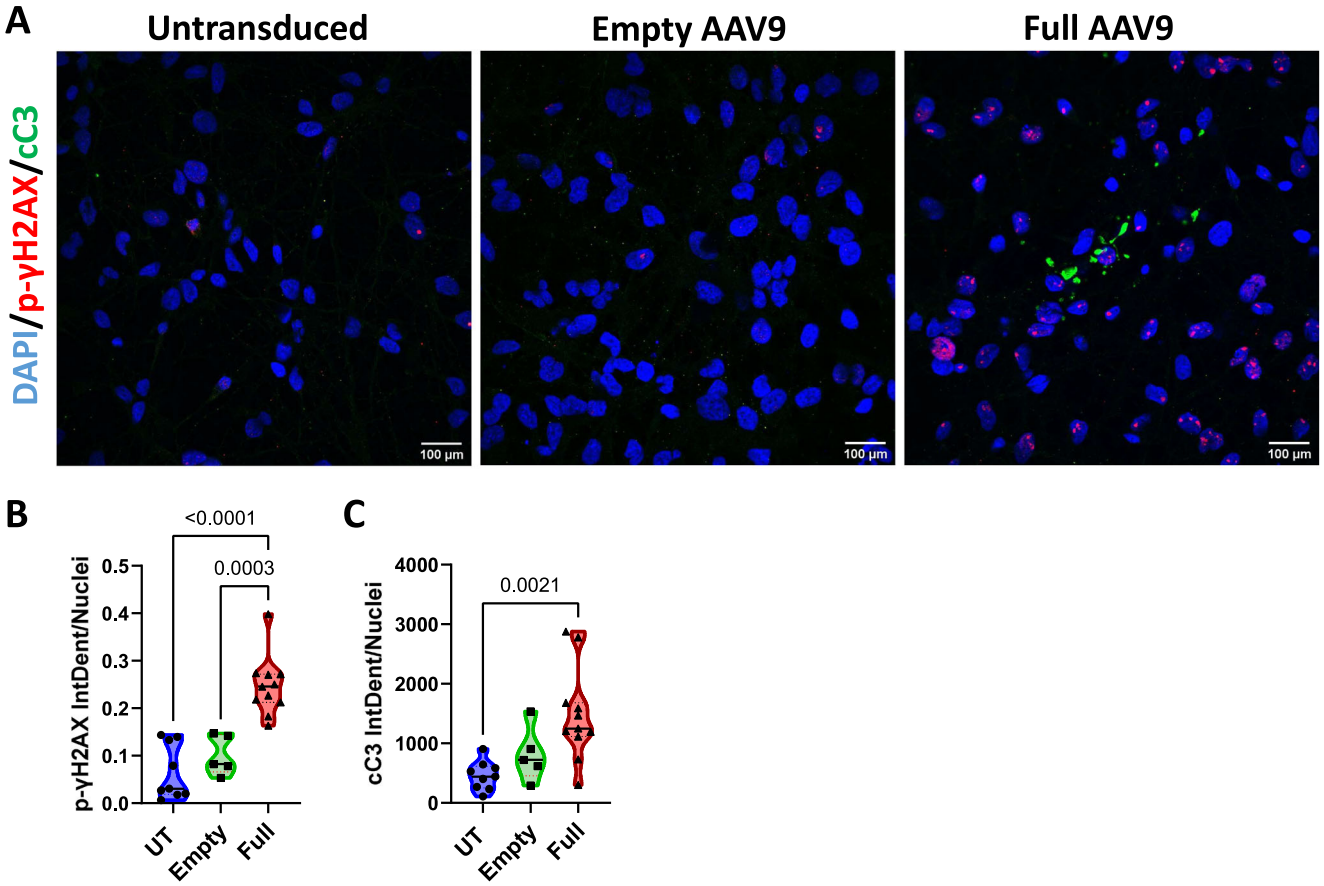

Fig. 2 | AAV9-mediated transduction activates functional DNA damage responses and apoptosis in hiPSC-derived neurons. A Immunofluorescence staining of phospho-γH2AX (p-γH2AX, red) and cleaved caspase 3 (cC3, green) in hiPSC-derived neurons transduced with empty or full AAV9 for 48 h. Scale bar 100 µm. Violin plots showing the quantification of p-γH2AX (**B**) and cC3 (**C**) intensities. N = 9 coverslips for untransduced (UT), $n = 5$ coverslips for Empty and $n = 11$ coverslips for Full-treated wells across cultures from 4 independent experiments. Data points refer to average values from 3–5 fields of view (FOV) per coverslip. Statistical significance was determined by one-way ANOVA with Tukey post-hoc test. Source data are provided as a Source Data file.

as innate immune sentinels. The response was characterized by an early activation of the p53 pathway, followed by a later upregulation of inflammatory and cell-stress signatures (Fig. 3E).

To further investigate AAV signalling in a setting that better recapitulates the complexity of the human brain, we evaluated the impact of AAV9 transduction in 3D human brain spheroids[34] cultured for 150 days and assessed at days two and five post-transduction (Fig. 4A). Single-cell transcriptomics of the transduced spheroids confirmed similar cell composition and GFP distribution to those observed in mixed 2D cultures (Figs. 4B–D, S8A), with higher GFP expression in astrocytes and oligodendrocytes as compared to neurons.

Transduction of brain spheroids also resulted in a time-dependent response, with early activation of the p53 pathway in both astrocytes and oligodendrocytes together with metabolic alterations, followed by an induction of inflammatory and IFN responses as well as cell-stress pathways such as apoptosis and unfolded protein responses (Figs. 4E, S8B). Similar responses were observed when transducing spheroids with other serotypes such as AAV Spk100 and AAV2 (Fig. S9), suggesting that these responses are independent of the capsid serotype used. Time-dependent induction of significant pathways was validated by qPCR of selected markers in hiPSC-derived astrocyte cultures transduced with AAV2-CAG-GFP, including the expression of p53-dependent genes (P21 and GDF15), interferon-stimulated genes (ISGs) (ISG15, OAS1 and IFI44L), as well as cytokines and chemokines (IL1B, CXCL8 and IL6) (Fig. S10). Together, these results highlight activation of type I IFN and inflammatory responses following initial activation of DDR in more complex 3D brain spheroids.

Inflammatory signatures are induced by different AAV serotypes and transgenes and depend on transgene expression

To gain further insight into the molecular mechanisms behind AAV-triggered toxicity, we dissected the contribution of the vector genome, transgene expression and sequence, respectively, in the observed signalling. For this purpose, brain spheroids were transduced with either AAV9 or Spk100 serotypes encoding various transgenes under the control of different promoters (Fig. 5A). These included GFP under the control of the ubiquitous CAG promoter or the liver-specific hAAT promoter, which is not expressed in CNS cells. Cells transduced with the CAG-carrying vector are exposed to both the vector genome and the transgene product (mRNA and protein), while cells transduced with the hAAT promoter are exposed to the vector genome, but do not express the transgene (Fig. S11A, B). Thus, this setting allows to study responses specifically triggered by the vector genome, given that the vector capsid alone was not associated with significant responses (Figs. 1, S3–S5). Moreover, we included vectors carrying the transgenes GAA (acid alpha glucosidase) and luciferase (gLUC) both under the CAG promoter to study responses triggered by transgenes other than GFP.

AAV-induced signalling was assessed at day five post-transduction by scRNAseq in the total cell population as well as in the transgene-positive and transgene-negative fractions in cells transduced with the CAG promoter, to highlight potential transgene-dependent effects (Fig. 5B–D). For panels 5B-D, the column corresponding to samples transduced with the hAAT promoter (Spk100-hAAT-GFP vector) is only represented in the analysis of the transgene-negative population (right panel), since no transcripts are derived from this expression cassette.

https://doi.org/10.1038/s41467-025-58778-3

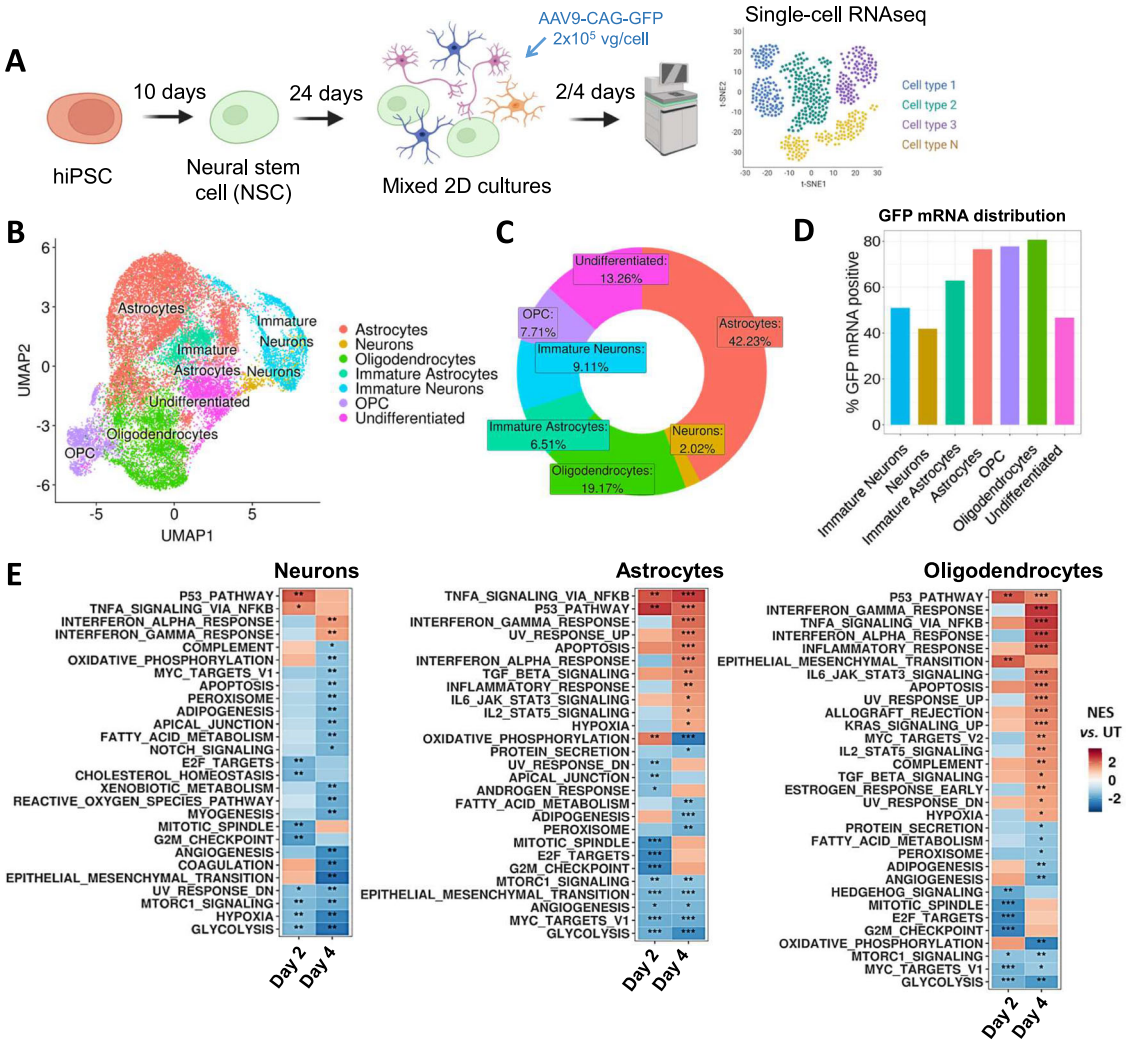

Fig. 3 | Single-cell transcriptomics of mixed neural cultures reveals time- and cell type- dependent activation of innate immunity pathways. A Scheme illustrating the differentiation process and transduction of hiPSC-derived mixed 2D cultures. Scheme created in BioRender. Costa, H. (2025) https://BioRender.com/u34k332. (**B**) UMAP plot of single-cell data generated with Seurat showing clustered untreated and treated samples from day 2. Cells are plotted in two dimensions using the UMAP dimensionality reduction technique and annotated by cell type. **C** Donut plot showing the frequency of each cell type in the UMAP shown in (**B**). **D** Quantification of the % of cells positive for GFP mRNA within each cell type for AAV9-treated samples on day 4. **E** Heat maps visualizing the enriched GSEA terms in total astrocytes, neurons and oligodendrocytes against the Hallmark gene set (Molecular Signatures Database). GSEA was performed on logFC pre-ranked gene lists obtained from gene expression levels of samples transduced with AAV9 compared to untransduced (UT) within each cell type using Kolmogorov-Smirnov test with FDR for multiple test correction (NES, normalized enrichment score; *, adjusted $P < 0.05$; **, adjusted $P < 0.01$; ***, adjusted $P < 0.001$).

Interestingly, the signalling triggered by the non-expressing Spk100-hAAT-GFP vector was overall milder compared to samples transduced with CAG-driven vectors and more evident in the more responsive astrocyte (Fig. 5B) and oligodendrocyte (Fig. 5C) cell subsets. Signalling in hAAT-transduced samples was limited to oxidative phosphorylation, p53 and DNA repair responses. These results suggest that the vector genome alone is sufficient for triggering the DNA-damage signalling, while transgene expression modulates additional pro-inflammatory pathways detected in cells transduced with vector containing the CAG promoter and thus expressing the transgene. This was also confirmed by qPCR of selected genes in hiPSC-derived neuron cultures, showing that only the induction of p53-dependent genes was maintained when using hAAT as a promoter as shown by the p21 expression (Fig. S11C), suggesting that part of the vector signalling, in particular inflammatory and type I IFN responses, are associated with transgene expression.

When focusing on the transgene mRNA-positive cells (Fig. 5B–D, middle panel), signalling was significant across all transgenes tested with the highest responses observed for the clinically relevant GAA transgene, suggesting that intrinsic characteristics of each transgene sequence may contribute to modulating the signalling. Of note, similar responses were observed in transgene-positive and negative populations in samples transduced with CAG-carrying vectors, suggesting a potential paracrine signalling between transduced and neighbouring non-transduced cells, or the presence of vector genomes in the transgene-negative populations that cannot be detected by RNA sequencing, contributing to activation of p53-dependent pathways and downstream effects.

Overall, our results reveal an early, vector genome-dependent activation of p53-mediated DNA damage responses, in complex cultures of human CNS cells upon AAV transduction, followed by a later induction of type I IFN and inflammatory pathways that seem to be enhanced by transgene expression.

AAV9-mediated CNS transduction induces pro-inflammatory and cell stress signalling in vivo

Because the extent of vector tissue distribution and transduction efficiencies differ between in vitro and in vivo settings, and the lack of

https://doi.org/10.1038/s41467-025-58778-3

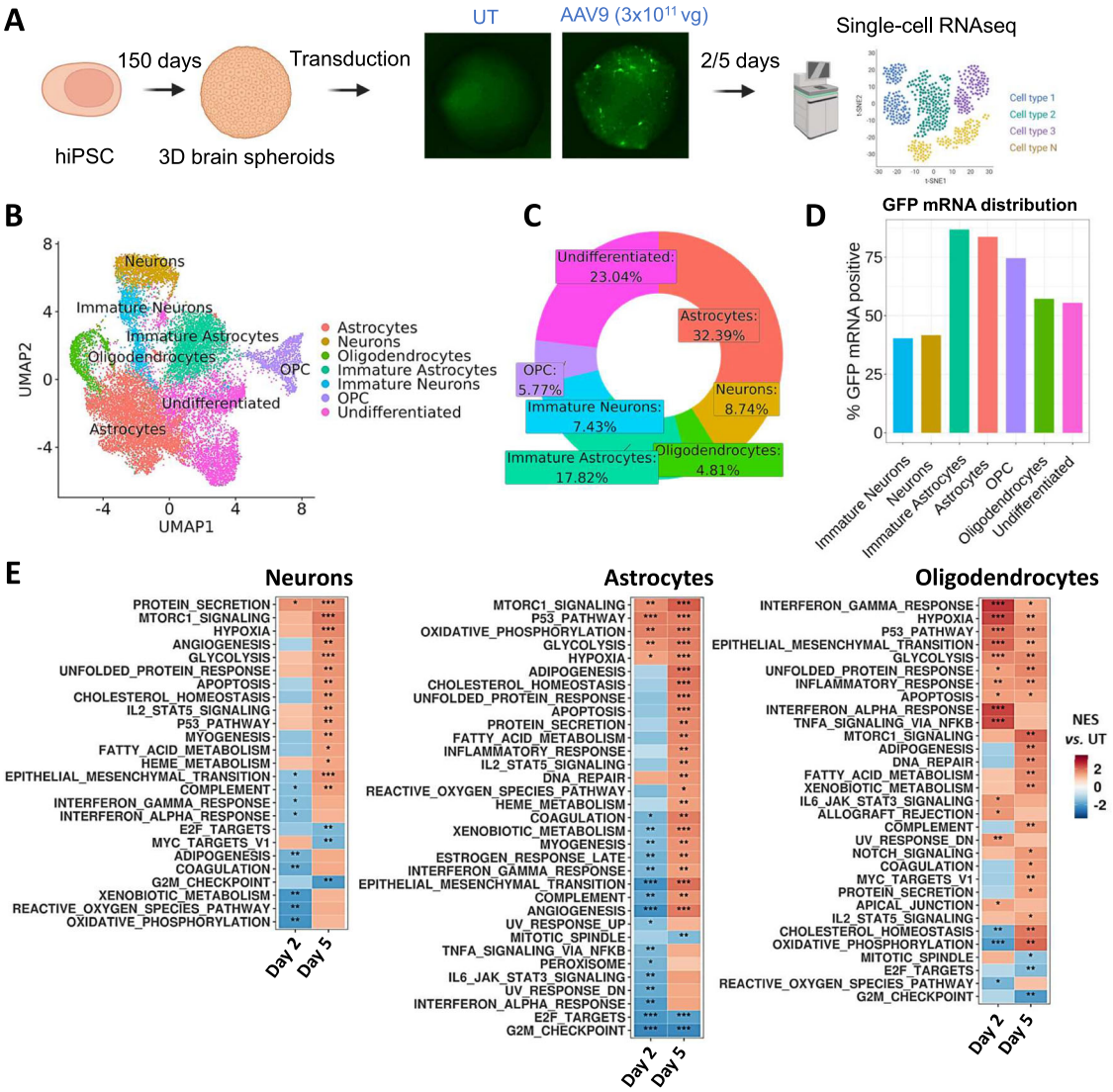

Fig. 4 | AAV transduction leads to a time-dependent activation of DNA damage and inflammatory responses in 3D spheroids. A Scheme illustrating the differentiation process and transduction of hiPSC-derived 3D brain spheroids. Scheme partially created in BioRender. Costa, H. (2025) https://BioRender.com/u34k332. **B** UMAP plot of single-cell data generated with Seurat showing untreated and treated samples clustered. Cells are plotted in two dimensions using the UMAP dimensionality reduction technique and annotated by cell type. **C** Donut plot showing the frequency of each cell type in the UMAP shown in (**B**). **D** Quantification of the % of cells positive for GFP mRNA within each cell type on spheroids transduced with AAV9 after 5 days. **E** Heat maps visualizing the enriched GSEA terms in total astrocytes, neurons and oligodendrocytes against the Hallmark gene set (Molecular Signatures Database). GSEA was performed on logFC pre-ranked gene lists obtained from gene expression levels of samples transduced with AAV9 compared to untransduced (UT) within each cell type using Kolmogorov-Smirnov test with FDR for multiple test correction (NES, normalized enrichment score; *, adjusted $P < 0.05$; **, adjusted $P < 0.01$; ***, adjusted $P < 0.001$).

immunological studies in the brain, we performed an in vivo study to assess the responses triggered upon intraparenchymal (IPa) AAV9 injection in mice. Adult male mice were bilaterally injected into the striatum with AAV9-CAG-GFP or vehicle ($n = 2$ mice/group respectively) and were sacrificed 28 days post-injection, a time-point at which robust transgene expression can be expected[35,36] and CNS toxicities have been reported[11,15,37], which in the DRG context have been shown to be transgene expression-dependent[38]. Striata were then dissected for the assessment of cell type composition and transcriptional changes by single-nucleus RNAseq (snRNAseq) (Figs. 6A, S12). Cluster analysis of cell populations revealed the presence of different neuron subsets, astrocytes, oligodendrocytes and microglia, with no relevant differences potentially associated with the treatment (Fig. 6B, C). The distribution of GFP mRNA expression across cell populations was also analysed (Fig. 6D).

Pathway analysis showed the induction of common pathways between mice and hiPSC-derived CNS models, including type I and II IFN responses, in particular in glia cell subsets, as well as oxidative phosphorylation and several terms associated with DNA stress responses including UV response, DNA repair, apoptosis and the p53 pathway mainly observed in the neuronal populations (Figs. 6E, S13). For side-by-side comparison of human and murine datasets, we generated a GSVA heatmap of common pathways enriched across our different in vitro models and murine datasets, showing that samples clustered together according to cell-type and treatment and independently of the species of origin, showing high clustering scores for pathways including IFN response, p53 pathway, inflammatory signalling, complement responses or apoptosis (Fig. S13).

To confirm the induction of DNA damage signalling in the transduced tissue in vivo, we performed a co-localization staining analysis of markers p-γH2AX for DNA responses, together with NeuN to identify neurons, Sox9 for astrocytes[39], or Iba1 for microglia, in mouse brains injected in the striatum with IPa injection of either AAV9-CAG-GFP or vehicle, and euthanized four weeks after the injection (Fig. 7, Fig. S14).

https://doi.org/10.1038/s41467-025-58778-3

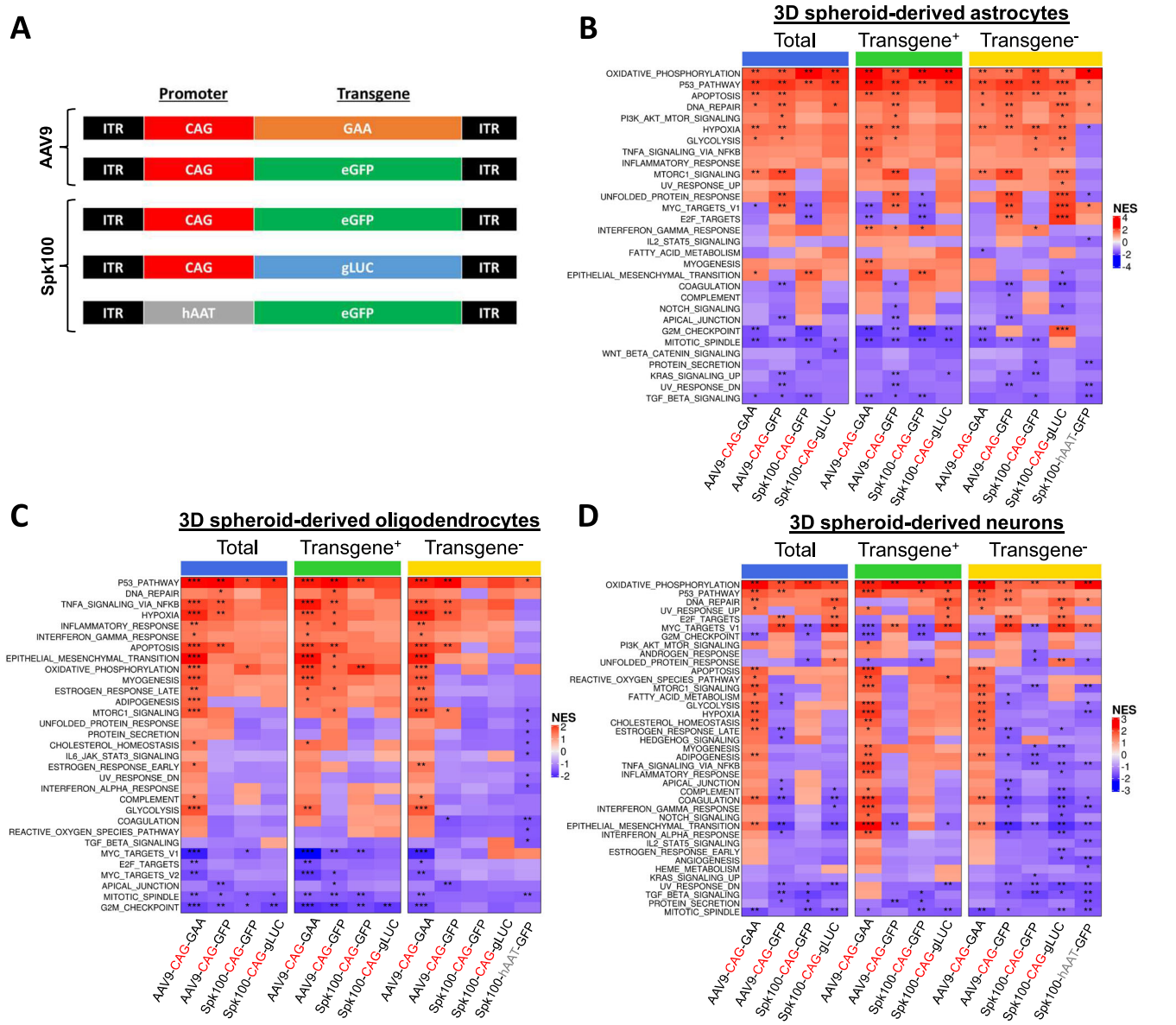

Fig. 5 | Inflammatory signatures are induced by different AAV serotypes and transgenes and depend on transgene expression. A Combinations of promoters and transgenes used to transduce 3D spheroids. Heat maps visualizing the enriched GSEA terms in (**B**) astrocytes, (**C**) oligodendrocytes, and (**D**) neurons either in the total population (left panel) or only in cells positive or negative for transgene mRNA (middle and right panels respectively) against the Hallmark gene set (Molecular Signatures Database) compared to untransduced controls within each cell type using Kolmogorov-Smirnov test with FDR for multiple test correction. The ubiquitous CAG promoter is highlighted in red (all panels) whereas the non-expressed hAAT promoter is coloured in grey (Transgene$^-$ panel only). (NES, normalized enrichment score; *, adjusted $P < 0.05$; **, adjusted $P < 0.01$; ***, adjusted $P < 0.001$).

Similar to our in vitro findings, IF analyses of striatal brain sections showed formation of p-γH2AX foci in AAV9-CAG-GFP-injected compared to vehicle-injected mice, which mainly co-localized with NeuN$^+$ neurons (Fig. 7A, C), consistent with our in vitro observations that neurons are more sensitive to DNA damage responses. AAV9-injected animals also showed increased presence of GFAP$^+$Sox9$^+$ astrocytes (Fig. S14A–C) and Iba1$^+$ microglia (Fig. S14D, E), in line with the induction of pro-inflammatory pathways detected by snRNAseq in these cell populations in injected animals. Iba1$^+$ cells expressed microglia activation markers such as Galectin-3[40] (Fig. S14D, F) and Gasdermin D (GSDMD)[41] (Fig. S14G, H). Finally, the presence of infiltrating CD45$^+$ and CD3$^+$ cells was also detected by IF in AAV9-injected striatum (Fig. S14I, J), altogether indicating the induction of gliosis and recruitment of immune cells.

Overall, our findings reveal the activation of innate signalling pathways, gliosis and DNA damage responses when AAV is administered into the brain in vivo, further supporting and validating the relevance of our findings in the context of hiPSC-derived CNS cells.

AAV-induced pro-inflammatory signalling and apoptosis are dependent on p53

We next sought to dissect the cellular sensors potentially involved in the different pathways triggered by AAV transduction. Our transcriptomic analysis revealed induction of antiviral IFN signalling in AAV-transduced human and murine CNS cells in vitro and in vivo, respectively (Figs. 3, 4 and 6). Type I IFN can arise from TLR9 activation in cells such as plasmacytoid dendritic cells (pDCs) in the context of AAV administration in a CpG-content dependent manner[22,42]. The hAAT and CAG promoters that we used to dissect AAV signalling in vitro differ in CpG content (Fig. S15). As the CpG content of the AAV vector sequence has been shown to be an important modulator of cellular responses against transduced cells in vivo[42,43], this could

https://doi.org/10.1038/s41467-025-58778-3

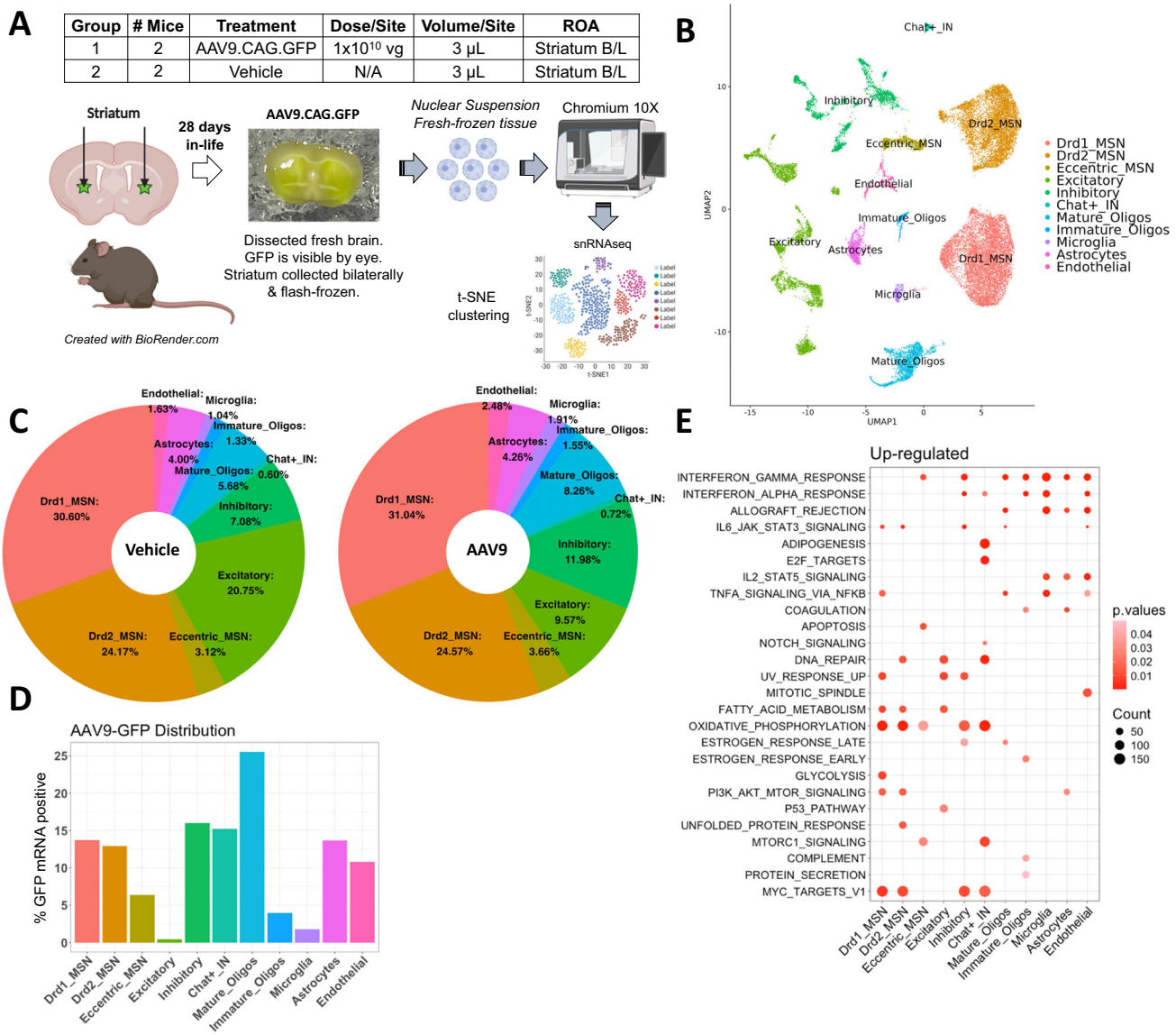

Fig. 6 | AAV9-mediated CNS transduction induces pro-inflammatory signalling in vivo. A Study design. AAV9 vector or vehicle control were stereotactically injected bilaterally (B/L) into striatum of adult C57BL/6 J male mice. Striatum was collected 28 days post-injection for snRNAseq processing. Scheme partially created with BioRender. Dzhashiashvili, Y. (2025) https://BioRender.com/e92m679. **B** UMAP plot of mouse striatum single-nucleus data generated with Seurat. Cells from vehicle and AAV9-treated mice are clustered and plotted in two dimensions using the UMAP dimensionality reduction technique and annotated by cell type. **C** Donut plot showing the frequency of each cell type per treatment group. **D** Quantification of the percent of cells positive for GFP mRNA within each cell type. **E** Dot plots visualizing the enriched up-regulated GSEA terms in different cell types against the Hallmark gene set (Molecular Signatures Database). GSEA was performed on logFC pre-ranked gene lists obtained from gene expression levels of samples transduced with AAV9 compared to vehicle within each cell type. Enriched pathways are ranked according to their normalized enrichment scores. Significance testing was performed with fgsea package in Bioconductor, comparing gene set enrichment scores to a null distribution of random permutations of the gene rankings. *P*-values were adjusted using the Benjamini-Hochberg correction to control FDR.

contribute to the differences in signalling induced by the different expression cassettes through TLR9 sensing. To test this hypothesis, we transduced iPSC-derived astrocytes with different AAV serotypes following pre-treatment with a TLR9 inhibitor (TLR9i). No impact of TLR9 blockade in the induced signalling was observed compared to AAV alone (Fig. S16A–E). In agreement, an AAV2 vector harbouring a modified TLR9-ihibitory sequence, AAV2-CMV-GFP-io2 (AAV2.io2) that has been shown to attenuate cellular responses to AAV[44], did not decrease the pro-inflammatory signalling induced by transduction (Fig. S16F, G). The use of single-stranded or self-complementary vectors has also been shown to modulate TLR9 activation[45,46]. However, no significant differences in gene induction were observed between single-stranded AAV9-CAG-GFP (ssAAV9) and self-complementary AAV9 (scAAV9) in astrocytes (Fig. S17A, B). Altogether, these results suggest that TLR9 is not a major mediator of innate signalling in hiPSC-derived neural cell types in vitro.

AAV-triggered type I IFN responses have also been shown to depend on the MDA5/MAVS dsRNA sensing pathway in different cell lines and primary human hepatocytes[47]. To explore the role of RNA sensing in our models of the human CNS, we transduced hiPSC-derived astrocytes with a lentiviral (LV) vector encoding two different MAVS-targeting guide RNAs and the Cas9 nuclease (LV-gRNA/Cas9). As controls, cells were transduced with Cas9-only encoding LV. Two days after LV-transduction, cells were transduced with AAV6-CAG-GFP (Fig. S18), which induces similar signalling as AAV2 (Fig. 1). MAVS knockout did not prevent the induction of p53 nor cytokine responses

https://doi.org/10.1038/s41467-025-58778-3

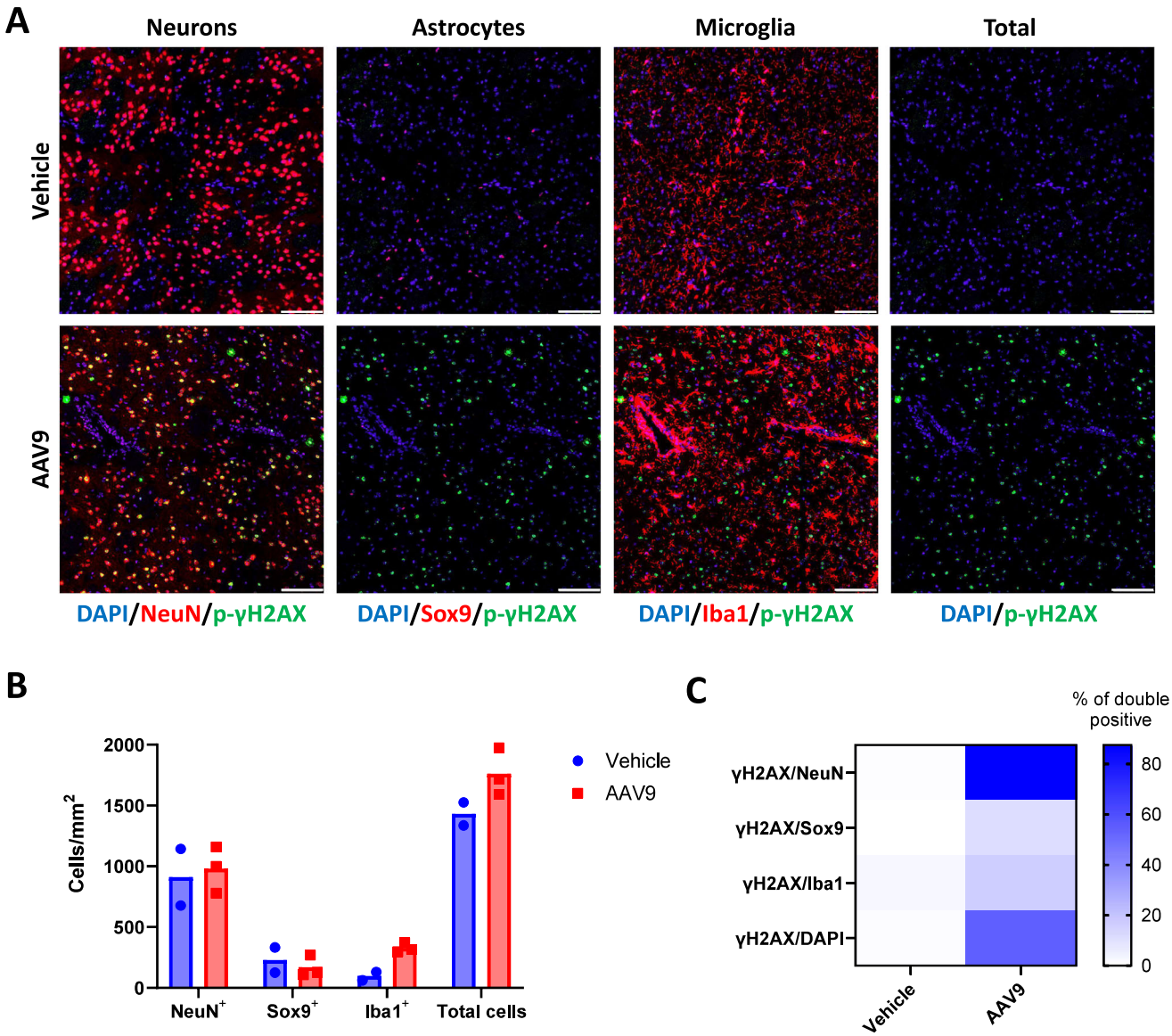

Fig. 7 | AAV9-mediated CNS transduction induces functional DNA damage responses and gliosis in vivo. A Representative IF images of p-γH2AX staining (green) on striatum sections together with the neuron marker NeuN, the astrocyte marker Sox9 or the microglia marker iba1 in vehicle-treated mice ($n = 2$) compared to mice receiving intraparenchymal injection of an AAV9-CAG-GFP vector ($n = 3$) 4 weeks before sacrifice. Scale bar 100 μM. **B** Quantification of the total number of NeuN$^+$, Sox9$^+$, Iba1$^+$ or total DAPI$^+$ cells per section per animal from vehicle- ($n = 2$) and AAV9-treated ($n = 3$) animals. **C** Heatmap representation of the average percent values of NeuN$^+$, Sox9$^+$, Iba1$^+$ or total DAPI$^+$ cells that are positive for p-γH2AX in striatum sections from vehicle- ($n = 2$) *vs.* AAV9-treated ($n = 3$) animals. Source data are provided as a Source Data file.

in terms of p21 and IL-1β mRNA expression levels (Fig. S18B), but significantly diminished the expression of ISGs (Fig. S18C), suggesting that RNA sensing through MAVS specifically drives AAV-induced type I IFN responses but not the pro-inflammatory signalling.

To test the role of p53 in the induction of inflammatory cytokines and chemokines in hiPSC-derived astrocytes, cells were transduced with a LV vector encoding for a dominant negative p53 suppressor peptide GSE56 (LV-GSE56)[26] or with a LV-BFP (blue fluorescent protein) control 2 days prior to transduction with AAV2-CAG-GFP (Fig. 8A). Induction of p53-dependent genes, ISGs and pro-inflammatory genes was assessed 4 days post-AAV transduction by qPCR (Fig. 8B–D). As expected, inhibition of p53 through GSE56 expression prevented p21 induction by AAV2 (Fig. 8B). Interestingly, while GSE56 only partially prevented induction of ISGs (Fig. 8C), it completely abrogated the inflammatory signalling, as measured in terms of CXCL8 and IL-1β gene expression (Fig. 8D). Importantly, preventing AAV-induced p53 activation also curbed vector-induced toxicity in hiPSC-derived neurons, as evidenced by the rescue of apoptotic cC3 staining (Fig. 8E–G) and reduction of lactate dehydrogenase (LDH) release (Fig. 8H) in cells expressing the GSE56 peptide.

Together, results indicate that AAV transduction activates RNA-dependent type I IFN signalling and p53-related neurotoxic inflammation in hiPSC-derived CNS cells.

AAV-triggered neurotoxicity can be prevented through p53 or cGAS/STING inhibition

Finally, we tested a series of inhibitors of innate immune sensors and cell-stress pathways in vitro and in vivo to further understand the responses triggered downstream of p53 and identify strategies to prevent target-cell toxicity.

We first tested different inhibitors of pathways previously suggested to play a role in AAV toxicities such as the complement

https://doi.org/10.1038/s41467-025-58778-3

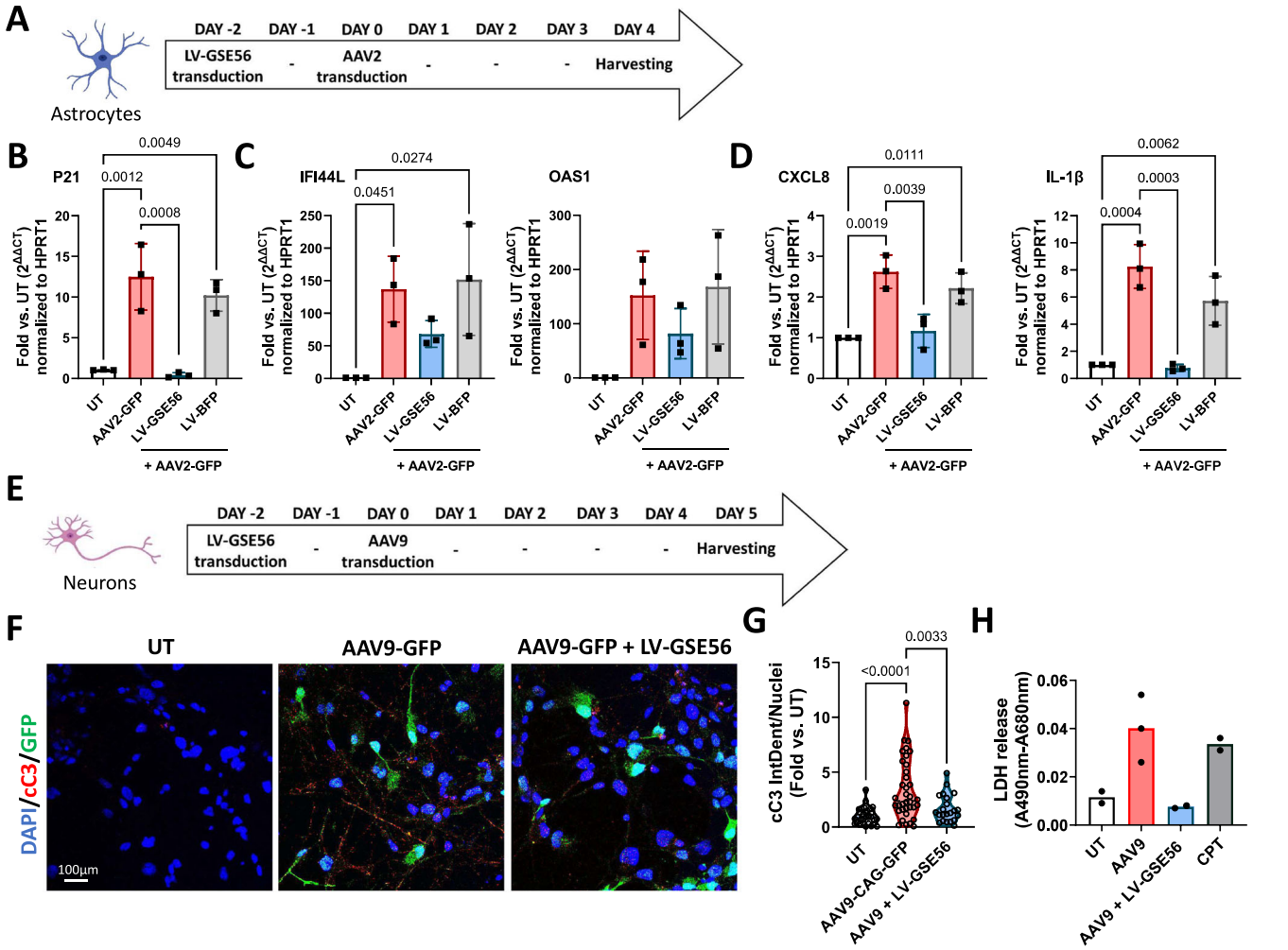

Fig. 8 | AAV-induced pro-inflammatory signalling and apoptosis are dependent on p53. A Scheme of the experimental design for the transduction of hiPSC-derived astrocytes. Analysis of (**B**) P53-dependent genes, (**C**) ISGs and (**D**) cytokines and chemokines by qPCR in astrocytes at day 4 post-AAV2 transduction. Data are shown as mean ± SD between 3 independent experiments, each performed in technical duplicate. Statistical significance was determined by one-way ANOVA with Tukey post-hoc test. **E** Experimental design for the transduction of hiPSC-derived neurons. For A and E, schemes were partially created with Biorender. Costa, H. (2025) https://BioRender.com/u34k332. **F** Immunofluorescence staining of cC3 (red) in hiPSC-derived neurons at day 5 post-AAV9 transduction. Scale bar 100 µm. **G** Violin plot showing the quantification of cC3 staining. $N = 31$ FOVs for untransduced (UT), $n = 36$ FOVs for AAV9-CAG-GFP and $n = 22$ FOVs for AAV9-GFP + LV-GSE56 across cultures from 3 independent experiments, 3 coverslips per condition per experiment. Data points refer to individual fields of view. Statistical significance was determined by one-way ANOVA with Tukey post-hoc test. **H** LDH release assay performed on supernatants from neurons collected on day 5 post-AAV transduction. Data are shown as mean between 2 experimental replicates for all conditions except for AAV9 ($n = 3$). Source data are provided as a Source Data file.

pathway[48] or the unfolded protein response[49] in iPSC-derived astrocytes. However, none of the tested inhibitors prevented AAV-induced inflammation in these cells (Fig. S19). Instead, blockade of cGAS-STING signalling with the inhibitor H151, or IL-1R-mediated inflammation with Anakinra, efficiently prevented the induction of pro-inflammatory responses in vitro (Fig. 9A, C). These drugs had no impact on the expression of p53-dependent genes p21 and GDF15 (Fig. 9B), indicating that both STING and IL-1R signalling are activated downstream of p53. In agreement with this hypothesis, preventing p53 activation through GSE56 expression inhibited CXCL8 secretion to a similar extent as H151 and Anakinra in transduced cells (Fig. 9E). Moreover, these inhibitors reduced the expression of pro-inflammatory genes but did not affect the induction of ISGs (Fig. 9D). This confirms that distinct pathways are responsible for the inflammatory and the type I IFN signalling, shown here to be regulated by p53 and MAVS respectively. Importantly, preventing STING activation rescued AAV-induced cell death in hiPSC-derived 2D neuronal (Fig. 9F, G) as well as in mixed neuronal-glial cultures (Fig. 9H, I).

Given the apical role that the p53 responses seem to have on AAV-triggered inflammatory signalling in vitro, we sought to further assess its impact on glial cell activation in vivo. For this purpose, we took advantage of a transgene-silent vector harbouring the coagulation factor IX (FIX) transgene under the control of the liver-specific hAAT promoter that activated mainly DNA damage-related responses in the human CNS spheroids (Fig. 5). Mice were injected with the vector in the striatum with concomitant intraperitoneal administration of pharmacological inhibitors for p53 (pifithrin-α), cGAS (RU.521) or STING (H151), followed by assessment of gliosis on striatal sections 8 weeks post-injection (Fig. S20).

An increase in $Iba1^+$ and $GFAP^+$ cells was observed in mice having received the vector (Fig. S20B, C). Moreover, all three treatments decreased the presence of $GFAP^+$ cells in the striata compared to mice injected with AAV only, while they had no effect on the $Iba1^+$ population. NeuN staining indicated absence of neurotoxicity in terms of percentage of $NeuN^+$ cells. These results suggest that, in mice, AAV-mediated CNS transduction can activate gliosis even in a context of low or absent transgene expression when using the hAAT promoter, and

https://doi.org/10.1038/s41467-025-58778-3

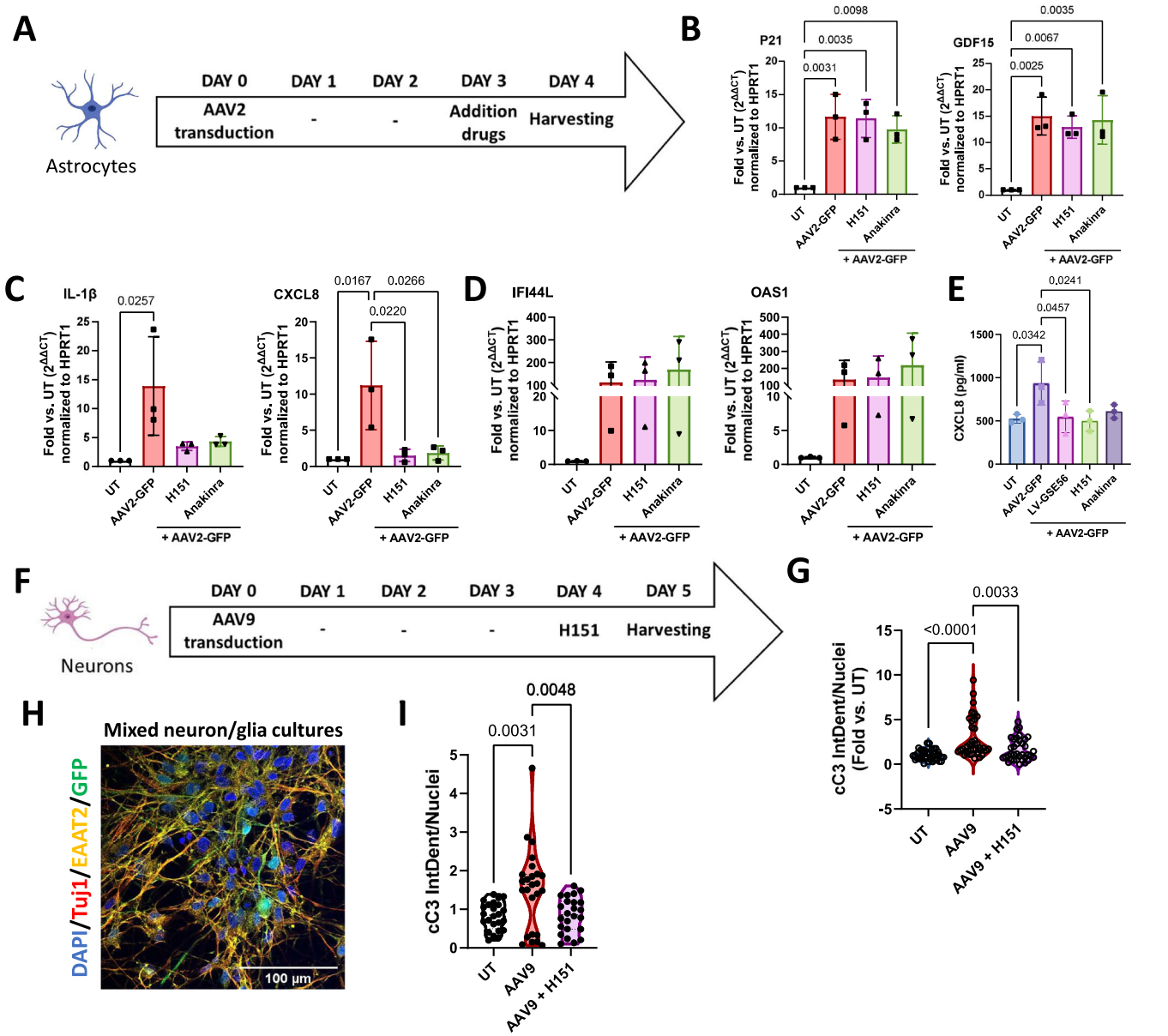

Fig. 9 | AAV-induced signalling involves STING and IL-1R downstream of p53. **A** Experimental design for the treatment of hiPSC-derived astrocytes. Analysis of (**B**) p53-dependent genes, (**C**) cytokines and (**D**) ISGs by qPCR in hiPSC-derived astrocytes at day 4 post-AAV2 transduction. Data are shown as mean ± SD between 3 independent experiments. Statistical significance was determined by one-way ANOVA with Tukey post-hoc test. **E** Quantification of CXCL8 in culture supernatants from hiPSC-derived astrocytes measured by ELISA as mean ± SD between 3 independent experiments. Statistical significance was determined by one-way ANOVA with Bonferroni post-hoc test. **F** Experimental design for the treatment of hiPSC-derived neurons. For (**A**) and (**F**), schemes were partially created with Biorender. Costa, H. (2025) https://BioRender.com/u34k332. **G** Quantification of cC3 staining in hiPSC-derived neurons treated as in F harvested at day 5 post-AAV9 transduction. $N = 40$ FOVs for untransduced (UT) and AAV9, $n = 36$ FOVs for AAV9 + H151, across cultures from 3 independent experiments, 3 coverslips per condition per experiment. Data points refer to individual fields of view. (**H**) Immunofluorescence staining of the neuron marker Tuj1 and the astrocyte marker EAAT2 in mixed 2D cultures transduced with GFP. **I** Quantification of cC3 staining in hiPSC-derived mixed 2D cultures treated as in F harvested at day 5 post-AAV9 transduction. $N = 24$ FOVs for untransduced (UT) and AAV9 + H151, $n = 25$ FOVs for AAV9, across cultures from 2 independent experiments, 3 coverslips per condition per experiment. Data points refer to individual fields of view. For (**G**) and (**I**), statistical significance was determined by one-way ANOVA with Tukey post-hoc test. Source data are provided as a Source Data file.

that these responses are not unique to the GFP transgene. Gliosis could be partially modulated through pharmacological inhibition of p53 or of the cGAS-STING pathway, highlighting that vector genome sensing contributes to the activation of local innate immune cells, particularly astrocytes.

Together, these results indicate that AAV-mediated CNS-cell transduction triggers inflammatory and type I IFN responses through two distinct and independent mechanisms mediated by p53 and MAVS respectively, and identifies STING-mediated signalling as a target to prevent AAV-induced neurotoxicity and gliosis downstream of p53-dependent responses.

Discussion

Our work identifies nucleic acid sensing as a trigger of innate immunity and cell death markers upon AAV transduction of CNS cells, providing timely insight into the molecular mechanisms potentially contributing to the sub-clinical to severe neurological adverse events that do not seem to involve adaptive cell-mediated immune responses[8,14,15].

Since the late 90's there has been an increasing trend in the number of clinical trials using AAV vectors to deliver transgenes[50], thanks to initial promising results of intravenous gene therapies targeting the liver for various metabolic diseases[51], a setting in which the required doses are relatively low and AAV has shown a safe immunogenicity profile[2]. AAV vectors constitute a versatile tool to target multiple organs thanks to the existence of a variety of AAV serotypes with different tissue tropism. Indeed, a number of trials have reported safe AAV administration, including into the brain, leading to the approval of Upstaza for the treatment of aromatic l-amino acid decarboxylase deficiency[52]. However, targeting the CNS through systemic administration remains challenging and requires vector doses 10- to 100-times higher than those used to target the liver[2,3]. At such high doses, AAV administration has resulted in a variety of toxic effects[53]. A recent meta-analysis of 255 AAV clinical trials reported a total of 11 patient deaths across 8 trials, and 30 clinical holds, 18 of which were due to toxicity findings, with hepatotoxicity, thrombotic microangiopathy and neurotoxicity being the most prominent serious adverse events[50]. Furthermore, immune reactions triggered by the vector capsid or transgene product can also impact on the efficacy of the therapy[1,13].

Although the CNS is typically considered an immune-privileged site, it contains its own subsets of innate immune cells, primarily microglia and astrocytes, which can promote innate immune functions in response to microbial insult[54]. Moreover, neuron damage caused by viral infection may further promote glial cell activation and contribute to neurotoxicity[55]. Previous studies have shown the involvement of TLR sensing of the AAV capsid and genome by antigen presenting cells (APCs) in the establishment of adaptive responses against the vector[20,45,56]. However, it has been difficult to address the potential contribution of these innate immune responses to AAV-mediated gene delivery in the context of the human brain.

Our studies with various serotypes and transgenes show that AAV transduction triggers early DNA damage responses and apoptosis signatures followed by pro-inflammatory and type I IFN signalling in hiPSC-derived neurons and glial cells, when using genome-full vector preparations. Overall, we observed that the number of significantly upregulated genes contributing to a given pathway was dependent on the level of transduction by each serotype correlating with the delivery of higher vector genomes, rather than on capsid composition, given the absence of signalling by empty capsids. Moreover, upregulation of signalling pathways seemed more significant in the 3D in vitro model compared to the 2D mixed cultures, suggesting potential cross-talk and paracrine effects of AAV signalling across cells of the human CNS. However, these differences could also result from the longer transduction time of brain spheroids or their longer differentiation, yielding higher maturation stages. Alternatively, an MOI effect could also account for some of the differences as the outer cells in the spheroids are more highly transduced compared to the inner ones, although single-cell analyses showed a similar percentage of GFP^+ cells across 2D and 3D cultures.

DNA damage responses was the first pathway induced upon AAV transduction across our in vitro experiments in human neural cells, involving the activation of several p53-dependent genes and formation of DDR foci. Studies indicate that DDR components of the MRN complex are recruited on the viral inverted terminal repeat (ITR) regions that flank the therapeutic expression cassette in the vector genome[57]. In our studies, the vector-induced DDR seems to persist up to five days in culture and for at least 28 days in vivo. It is possible that although AAV circularizes over time, the ITRs are still recognized despite the episomal form. In fact, microinjection of human embryonic stem cells with oligonucleotides containing the ITR sequence was sufficient to induce DDR and apoptosis in these cells[28]. Because DNA damage-induced inflammation is usually linked with the establishment of senescence in different contexts[58], it will be of interest to investigate whether the episomal persistence of the AAV vector genome could lead to senescence in the context of CNS-targeting therapies.

Several studies report the induction of DNA damage responses by wild-type AAV[57,59,60], as well as by recombinant AAV vectors[26,61] in different cell types. However, work has been missing in the context of the CNS. AAV vector genomes have been seen to colocalize with DNA-damage foci in the nucleus of cells such as HeLa or MRC5[61] and to activate p53-mediated signalling in human HSPCs ex vivo[26]. Yet, induction of DDR genes could not be observed in some cell lines such as 2-OS, Huh7 or A549[59], highlighting the importance of using relevant models when assessing AAV-derived signalling and toxicity. In addition, p53 is mutated or altered in multiple immortalized cell lines[62,63], resulting in altered DDR.

Vector-induced activation of DDR foci, inflammatory markers and gliosis were confirmed in vivo in mice in the context of IPa injection. These results suggest that studies in hiPSC-derived CNS models are relevant to predict pathways triggered by AAV vectors in vivo and are not just reflecting high exposure of cells to the vector in the in vitro setting. Nevertheless, vector signalling as shown by the number of induced GSEA terms, was overall lower in mice, either due to the potentially lower transduction levels achieved compared to in vitro transduction at the administered AAV dose, or to different species-specific responses between mice and humans. Indeed, studies in animal models tend to be less predictive of the clinical outcomes when it comes to AAV vectors[64,65], further supporting the use of hiPSC-derived models. Despite these differences, glial cell subsets seemed to respond to transduction mainly through the induction of several pro-inflammatory and interferon signatures without incurring cell death, while neurons were more sensitive to DNA damage and prone to apoptotic signatures across the different in vitro and in vivo models. Similar susceptibility of neurons to inflammation-induced cell death has been observed in the context of the rare genetic autoinflammatory neurodegenerative Aicardi-Goutières Syndrome[66].

Importantly, the activation of inflammatory responses was not exclusive to the reporter transgene GFP, as the expression of the clinically relevant GAA transgene also led to significant alterations of several inflammatory pathways in 3D brain spheroids. Our in vitro and in vivo studies with various inhibitors indicate that part of the pro-inflammatory signalling is p53-dependent, suggesting the contribution of the DDR machinery in detecting the viral vector genome and triggering inflammatory signals through a mechanism that involves downstream activation of STING and IL-1R pathways. In agreement with this hypothesis, CNS transduction with a hAAT-carrying vector, which triggered mainly p53-dependent signatures in human brain spheroids, induced some degree of gliosis in murine striata that could be partially dampened by inhibiting p53 or the downstream signalling through cGAS-STING inhibition. We also observed that expression of the transgene played a role in the magnitude of the induced signalling, as shown by scRNAseq performed on hiPSC-derived 3D brain spheroids transduced with either the ubiquitous CAG promoter or the liver-specific hAAT promoter. Previous work has suggested a role for transgene over-expression in DRG toxicity[38]. Here, we show that transgene expression is associated with enhanced inflammatory and anti-viral signalling in vitro as compared to conditions in which the transgene is not expressed, suggesting a link between transgene expression, inflammation, and neurotoxicity. Further experiments will help elucidate the extent to which transgene expression can further impact the induction of gliosis in vivo.

DNA damage responses induced at high AAV vector doses, as a result of high VGCN, could mediate neural cell loss through intrinsic apoptotic signalling, together with the onset of local inflammation due to release of cytokines and chemokines. In fact, induction of the cell death marker cC3 could be prevented in vitro by p53 inhibition with GSE56, but also by downstream inhibition of STING and IL-1R. This is in line with previous reports showing the induction of apoptosis in a

cGAS-STING-dependent manner upon viral CNS infection[67]. Interestingly, a recent study has also reported the induction of IL-1R signalling in pDCs recruited into the liver upon AAV gene transfer, and its involvement in the induction of transgene-specific T cell responses, which could be prevented by IL-1R blockade with Anakinra[21]. Although Kumar and colleagues show that IL-1R signalling is relevant in the context of pDCs, whether such signalling pathways are also induced in the tissue target cells such as hepatocytes, as we have observed in the context of the CNS, and what are the sensors leading to induction of the IL-1R pathway in these cells remains to be determined.

As inhibiting the tumour suppressor p53 in vivo may elicit relevant safety concerns, the neuroprotective effects associated with STING inhibition that we identify in this study provide alternatives to be tested to prevent AAV gene therapy-associated inflammation and neurotoxicity. Moreover, the duration of the insult, which is not easy to predict in vitro, will be important to consider in the development of protocols based on transient immunomodulation. Links between IL-1 signalling and p53 have been reported in the context of tumour cells[68,69], and the cGAS-STING axis is increasingly linked to DNA damage[70], although the exact triggers of this pathway in the context of AAV-mediated CNS transduction remain to be defined. In agreement with the in vitro data suggesting that STING activation is downstream of p53, transduction-triggered gliosis was modulated to a similar extent by inhibition of p53, cGAS, or STING during and post-vector infusion in vivo in the context of a transgene-silent AAV that elicits signalling through vector genome sensing. Interestingly, the cGAS-STING signalling axis has been recently shown to drive chronic inflammation and functional decline during ageing in mice, with neuroprotective effects achieved using the H151 inhibitor[71].

While inhibiting both STING and IL-1R led to reduced expression of pro-inflammatory genes and was sufficient to reduce cell death staining in hiPSC-derived neurons and mixed cultures, these treatments had no impact on AAV-triggered type I IFN signalling that instead seemed to be dependent on MAVS-mediated RNA sensing, consistent with results previously obtained in HeLa cells[47]. It is possible that type I IFN activation could be tolerated to some extent, as anti-inflammatory drugs have been shown to prevent neurotoxicity in in vitro models of the human CNS[66] and to alleviate symptoms of rare genetic autoinflammatory diseases[72–74] without impacting the type I IFN scores typically associated with these pathologies. Of note, MAVS depletion consistently led to increased inflammatory signalling upon AAV transduction in hiPSC-derived astrocytes. While the mechanistic basis remains to be elucidated, MAVS depletion could potentially lead to alterations affecting inflammation indirectly due to its mitochondrial localization, or some priming of the cells could occur in the absence of physiological RNA sensing rendering them more reactive to incoming vectors.

Differences in CpG content between hAAT and CAG promoters could also influence the breath of immune activation. Previous work had identified TLR9, which recognizes unmethylated CpG sequences present in viral or bacterial but not mammalian DNA, as the sensor involved in the induction of type I IFN responses in pDCs[20,22]. However, here we show that type I IFN and inflammatory responses in CNS cells depend on a different mechanism, as TLR9 blockade could not prevent these responses, differently from MAVS inhibition for type I IFN or p53/STING blockade for inflammatory responses. These results further suggest that the differences in signalling observed between CAG and hAAT-carrying vectors in vitro are due to expression of the transgene similar to what has been reported in the context of DRG toxicity[38].

Our findings reveal potential targets to modulate proinflammatory responses derived from the innate sensing of AAV vectors and improve neuroprotection. Further mechanistic studies to explore the link between the different identified nucleic acid sensors and side-by-side comparisons of the magnitude of inflammatory responses triggered in vivo by different promoters will help elucidate the contribution of vector genome sensing, innate immune activation and IFN responses to DRG neuron loss and brain toxicity observed in vivo upon systemic and IPa AAV delivery, respectively. Moreover, additional studies are warranted to explore in more detail the contribution of microglia to AAV-mediated effects in vitro and in vivo.

Overall, our work uncovers mechanisms through which the viral genome as well as transgene expression activate cell-autonomous responses, ultimately causing cell death pathway activation in neurons, as well as subsequent innate immune responses and gliosis, and identifies pharmacological strategies that can help mitigate this effect. Mechanistically, we propose a working model in which the incoming vector DNA first triggers a p53-dependent DNA damage response that will subsequently activate the cGAS/STING-mediated inflammatory signalling, contributing to gliosis in mice. Conversely, the type I IFN activation seems mainly driven by cytosolic RNA sensing that converges to the adaptor molecule MAVS in this context, potentially enhancing pro-inflammatory signalling as compared to conditions in which the transgene is not expressed. This study provides potential mechanistic links with the detection of cellular immunity[75] and rare clinical findings, such as MRI observations and DRG toxicity at high vector doses[12,13,16] in a reduced number of patients. Nevertheless, the contribution of cGAS/STING and MAVS pathways to vector sensing will benefit from further confirmations in genetic mouse models, and further studies will help to elucidate the clinical impact of these molecular findings, given some of the limitations of the in vitro and in vivo mouse models used. While not precluding the clinical utility of AAV vectors for the treatment of CNS disorders, this work highlights the relevance of cell-intrinsic and innate immune activation as a potential mediator of AAV immunogenicity and may inform future immunomodulatory strategies to improve outcomes of CNS-targeted AAV-based gene therapies.

Methods

Cell culture and differentiations

hiPSC culture. Human cells were used according to the guidelines on human research issued by the San Raffaele Scientific Institute Ethic Committee (protocol TIGET-HPCT). Healthy donor hiPSCs clones previously characterized [clone ND1.3[66,76] and clone ND2.2[77] were maintained in mTESR plus medium (Stemcell Techologies). hiPSC colonies were split using PBS 0,5 mM EDTA (Thermo Fisher Scientific).

hiPSC differentiation into neural stem cells (NSC). For neural induction, hiPSC colonies were detached with Accutase (Sigma-Aldrich), suspended as single cells, and plated on Matrigel (BD Pharmingen)-coated dishes (50,000 cells/cm^2) in mTESR plus medium in the presence of 10 µM of the Rho kinase inhibitor (Rock inhibitor) Y-27632 (Sigma-Aldrich). When the cell culture reached ≈90% confluence (usually 2 days after plating), the culture medium was replaced with knockout DMEM (Thermo Fisher Scientific) supplemented with knockout serum replacement (Thermo Fisher Scientific) together with 200 ng/ml of rhNOGGIN (R&D Systems) and 10 µM of SB431542 (Sigma-Aldrich). The medium was changed daily for the next 3 days. Thereafter, it was switched every other day to gradually expose the cells to increasing (1:3, 1:1, 3:1) ratios of NSC basal medium[78]. Two days after the final switch, cells were detached using Accutase and plated on Matrigel-coated dishes in NSC basal medium supplemented with 20 ng/ml human recombinant bFGF and 20 ng/ml human recombinant EGF (both from PreproTech) in the presence of 10 µM of Rock inhibitor Y-27632, according to the published Dual Smad inhibition protocol[78,79].

Differentiation of NSCs into mixed neuronal/glial cultures and pro-inflammatory astrocytes. Differentiations were performed as previously described[80–82]. Cells at the stage of NSCs were detached using Accutase and plated on Matrigel-coated dishes (20,000 cells/cm^2) in NSC basal medium supplemented with bFGF and EGF (day 0). During

the initial 4 days after plating, NSC medium was gradually replaced by an increasing ratio of glial differentiation medium, consisting of NSC basal medium supplemented with 10 ng/ml platelet-derived growth factor AA (PDGF-AA, Sigma-Aldrich), 10 ng/ml neurotrophin 3 (NT3, PreproTech), 10 ng/ml IGF-1 (PreproTech), 5 ng/ml hepatocyte growth factor (HGF, PreproTech), and 60 ng/ml 3,3,5-Triiodo-l-thyronine (T3, Sigma-Aldrich). From days 4 to 13, the glial differentiation medium was changed every other day. For the induction of astrocyte maturation, from days 14 to 34, the medium was switched to DMEM/F-12 Glutamax (Thermo Fisher Scientific) supplemented with N2 and B27 (both from Thermo Fisher Scientific), 10% foetal bovine serum (FBS) and 10 ng/ml leukaemia inhibitory factor (LIF, Sigma-Aldrich).

For experiments on mixed 2D cultures, cells were transduced on day 24 of the differentiation protocol from iNSCs. At this timepoint, neurons, astrocytes, and oligodendrocytes are simultaneously present[82]. For pro-inflammatory astrocyte enrichment, iNSCs were differentiated up to day 34, after which cells were detached with Accutase and passed in new Matrigel-coated wells to deplete neurons and oligodendrocytes from mixed cultures through mechanical dissociation and detach/replate steps for at least two passages before performing the transduction experiments[80].

Differentiation of NSCs into neurons. NSCs obtained through the Dual Smad inhibition protocol, as described above, were further differentiated into neurons with the STEMdiff Forebrain Neuron Differentiation Kit and maintained in culture with the STEMdiff Forebrain Neuron Maturation kit (both from StemCell Technologies) following manufacturer's instructions. Cells were used for transduction experiments after 21 days in maturation medium.

hiPSC differentiation into 3D brain spheroids. The generation of 3D spheroids was performed as previously described[34]. Briefly, hiPSCs were detached using Accutase and plated as single cells (3×10^6 cells/well) on AggreWell-800 plates (StemCell Technologies) in Essential 8 medium (Thermo Fisher Scientific) in the presence of 10 µM of Rock inhibitor Y-27632. After 24 h, hiPSC-derived embryoid bodies (EBs) were transferred in low attachment 10-cm dishes and cultured in Essential 6 medium (Thermo Fisher Scientific) with 10 µM SB431542 and 2.5 µM dorsomorphin (Sigma-Aldrich), by adding 5 µM IWP-2 (Selleckchem) at day 4 of differentiation. At day 5, culture medium was changed in Differentiation and Maintenance Medium (DMM) containing DMEM/F12 1:1 media (Thermo Fisher Scientific), B-27 supplement without vitamin A (1:50), N2 supplement (1:100), minimum essential media (MEM) non-essential amino acids (1:100; Thermo Fisher Scientific), GlutaMax (1:100; Thermo Fisher Scientific), 25 µg/ml human insulin (Sigma-Aldrich), 0.1 mM β-mercaptoethanol (Thermo Fisher Scientific), and penicillin/streptomycin. The DMM was supplemented with 20 ng/ml EGF, 20 ng/ml bFGF, and 5 µ M IWP-2 from day 5 to 24, by adding 1 µ M SAG (smoothened agonist, Sigma-Aldrich) at day 12. At day 25, the culture medium was switched in DMM supplemented with 60 ng/ml T3, 100 ng/ml biotin (Sigma-Aldrich), 20 ng/ml NT-3, 20 ng/ml BDNF (PeproTech), 1 µM cAMP (Sigma-Aldrich), 5 ng/ml HGF, 10 ng/ml human IGF-1, and 10 ng/ml PDGF-AA to induce glia differentiation. To favour glia maturation, the DMM medium was supplemented with 60 ng/ml T3, 100 ng/ml biotin, 1 µM cAMP and 20 µg/ml ascorbic acid from day 37 to 150.

Primary neuron culture. Cryopreserved human primary neurons from a human healthy brain were obtained from Innoprot. Cells were plated on poly-L-lysine-coated 48-well plates and cultured in complete Brainphys media (Stemcell Techologies).

Viral vectors

Empty and full AAV vectors serotypes Spk100, 1, 2, 5, 6 and 9 were kindly provided by Spark Therapeutics (Philadelphia, PA). AAV vectors were produced by transient transfection in HEK293 adherent culture and purified by double CsCl density gradient ultracentrifugation. Single-stranded and self-complementary AAV9-GFP vectors (scAAV9 and ssAAV9) were kindly provided by Dr. Giuseppe Ronzitti (Genethon). Vectors were produced using an adenovirus-ree transient transfection method and purified using affinity chromatography[83]. Purified AAVs were formulated under sterile conditions in buffer containing 180 mM Sodium Chloride, 10 mM Sodium Phosphate, 0.001% Pluronic F68, pH 7.3. Lentiviral vectors were produced by transient transfection in 293 T cells and were all VSV-g pseudotyped and concentrated by ultracentrifugation as already described[84]. Full vector titre were determined by qPCR as vector genomes (vg) per mL using primers directed against the transgene poly-adenylation signal region. The AAV titer was calculated by averaging results from 2 qPCR rounds with 3 different dilutions tested for each sample in each round. The purity of vector preparations was evaluated by SDS-PAGE gel. Empty capsid titre was determined by Sypro Ruby staining following SDS-PAGE[85]. Empty AAV9 and full AAV1, 2, 5, 6, 9 and Spk100 vector titre were simultaneously verified by side-by-side capsid imaging by western blot using an anti-AAV VP1/2/3 monoclonal antibody (Progen).

AAV transductions and drug treatments

AAV transduction for bulk and single-cell RNAseq and immunofluorescence staining. hiPSC-derived neurons (hiPSC clone ND1.3), astrocytes (hiPSC clone ND1.3) and mixed neural cultures (hiPSC clone ND2.2) were cultured in 48-well plates in 200 µl cell culture media. 100,000 – 200,000 cells per well were transduced with AAV vectors at the indicated MOI ($5 \times 10^4 - 1 \times 10^5$ vector genomes [vg]/cell for individual 2D cultures, 2×10^5 vg/cell for mixed cultures). At day 2 post-transduction, cells were collected for analysis (time-point day 2), or fresh media was replaced for cell collections at time-point day 4, when indicated. hiPSC-derived brain spheroids (from hiPSC clone ND2.2, 150 days of differentiation) were transferred individually to 48-well plates and transduced at 3×10^{11} vg/organoid in duplicates. Brain spheroids were transduced overnight in an incubator with orbital shaking. The day after, fresh medium was replaced and spheroids were further grown for 24 h or 96 h (time-points day 2 and day 5, respectively). For scRNAseq analysis, 2 mixed culture wells or spheroids/condition were dissociated and pooled at each time-point.

Combined treatment with lentiviral and AAV vectors. 100,000 hiPSC-derived mature neurons (hiPSC clone ND2.2) grown in 48-well plates were first transduced with lentiviral (LV) vectors encoding GSE56 or blue fluorescent protein (BFP) as control at MOI 5. Two days later, neurons were transduced with AAV9 ($2,5 \times 10^{10}$ vg/well) in duplicate wells for each condition. Five days after AAV9 transduction, neurons were fixed in 4% paraformaldehyde (PFA) for immunofluorescence (IF) analyses. 50,000 hiPSC-derived astrocytes (from hiPSC clone ND2.2) were plated in 48-well plates and transduced 24 h post-seeding with different LV vectors as indicated in each experiment, including GSE56- and BFP-encoding LV vectors, or a LV carrying the Cas9 nuclease together with two guide RNAs (gRNAs) against the MAVS gene (sequences ACAGGGTCAGTTGTATCTAC and AAGTTACCCCATGCCTGTCC), at MOI 5. Two days later, cells were transduced with AAV2 or AAV6 (5×10^{10} vg/well for an MOI of 250,000 due to cell proliferation) in duplicate wells for each condition. Transduced astrocytes were collected 4 days post-transduction for gene expression analysis by real-time PCR.

Treatment with pharmacological inhibitors. 100,000 hiPSC-derived astrocytes were transduced with AAV2 at 5×10^{10} vg/well. 72 h later, cells were treated with the 5 µM STING inhibitor H151 (InvivoGen) or 1 µg/µl IL-1 receptor (IL-1R) inhibitor Anakinra (SOBI). The day after, astrocytes were collected for gene expression analysis. 100,000 hiPSC-derived neurons were transduced with AAV9 ($2,5 \times 10^{10}$ vg/well), and

96 h later treated with 5 μM H151. The day after, cells were fixed in 4% PFA for IF analyses.

Flow cytometry

Cultured cells were detached using Accutase, washed and resuspended in PBS containing 2% FBS. 7-aminoactinomycin D (Sigma-Aldrich) was included during sample preparation according to the manufacturer's instructions to identify dead cells. GFP expression was analyzed with the FACS Canto III instrument (BD Biosciences) and analyzed with the FACS Express software (De Novo Software).

Immunofluorescence microscopy

For immunofluorescence (IF) analyses of in vitro cultures, cells were seeded on wells containing glass slides coated with the appropriate coating for each cell type and subsequently treated with viral vectors or pharmacological inhibitors as previously described. Cells were fixed with 4% PFA for 10 min at room temperature (RT) and permeabilized with 0.1% Triton X-100 for 20 min at RT. Samples were incubated for 30 min at RT in blocking solution containing 10% normal goat serum (NGS) in PBS, and stained overnight at 4 °C with cleaved caspase-3 (Asp175) antibody (rabbit polyclonal antibody, 1:200, Cell Signalling Technology), anti-phospho-Histone H2A.X (Ser139) antibody (mouse monoclonal antibody, 1:200, Sigma-Aldrich), EAAT2 antibody (E-1, mouse monoclonal antibody, 1:100, Santa Cruz Biotechnology) or anti-Tubulin β3 (TUBB3) antibody (mouse monoclonal antibody, 1:2500, Biolegend) diluted in 10% NGS. After three washes with PBS, samples were incubated with donkey anti-rabbit IgG Alexa Fluor 488 (1:500, A-21206, Thermo Fisher Scientific) or donkey anti-mouse IgG Alexa Fluor 555 (1:500, A-31570, Thermo Fisher Scientific) for 2 h at RT. Nuclei were stained with DAPI (Thermo Fisher) for 10 min at RT. Images were recorded using the TCS SP5 Leica confocal microscope, 60× with oil and analyzed with ImageJ software.

For staining of striatal sections, FFPE fixed brain tissue was sectioned at 5 μM, and slides were loaded onto the MACSima Imaging System four-well cassette (Miltenyi Biotech). Slides were subsequently stained with DAPI for 10 min and washed thrice with MACSima running buffer (Miltenyi Biotech). Tissues were then stained and imaged in a cyclical manner through subsequent rounds of staining and bleaching in the MACSima instrument. MACSima images were analyzed with MACS® iQ View Analysis Software (Miltenyi Biotech). A heat map representing the average percent values of p-yH2AX cells was generated with Prism. Refer to Supplementary Table 2 for details on antibodies, all used at 1:50 dilution.

Gene expression

Total RNA was extracted from cultured cells with the RNeasy Plus Micro kit (Qiagen) or ReliaPrep RNA Cell Miniprep System (Promega) according to the manufacturer's protocol. cDNA was generated using SuperScriptVILO cDNA Synthesis Kit (Thermo Fisher Scientific) according to manufacturer's instructions. Gene expression analysis was performed with commercial Taqman gene expression assays (Life Technologies). Refer to Supplementary Table 2 for details on the assays used. Human HPRT1 was used to normalize the total quantity of human cDNA input. Samples were run on the ViiA 7 Real-Time PCR System (Life Technologies). Gene expression was analyzed on QuantStudio™ Real-Time PCR Software. Relative quantification values were calculated as the fold-change expression of the gene of interest over its expression in the reference sample, by the formula $2^{(-\Delta\Delta Ct)}$.

Bulk RNAseq

Total mRNA was extracted from hiPSC-derived neurons or astrocytes in triplicates for each condition with ReliaPrep RNA miniprep system (Promega). RNA integrity was analyzed with the Agilent 2100 Bioanalyzer (Agilent Technologies, Santa Clara, CA). Libraries were prepared starting from 100 ng of total RNA per sample. The quality of raw paired-end reads was determined using FastQC, and read trimming was performed using Trim_galore to remove residual adapters and low-quality sequences. Trimmed reads were aligned against the human reference genome (GRCh38, p13) using STAR[86] v2.7.6a with standard input parameters, and only uniquely mapped reads were considered for downstream analyses. Reads were assigned to genes with featureCounts[87] v2.0.1, using the GENCODE primary assembly v35 gene transfer file as reference annotation for the genomic features. Transcript count matrices were then imported into the R statistical environment and processed by the R/Bioconductor package DESeq2 (Love et al., 2014) following the standard workflow. Genes with adjusted *P* values < 0.05 were considered as differentially expressed. Functional enrichment analysis was performed on the Hallmark gene set from the Molecular Signatures Database (MSigDB) using the Gene Sets Enrichment Analysis (GSEA) approach as implemented in the R/Bioconductor package clusterProfiler[88] v3.18, by pre-ranking genes according to log2 (fold-change [FC]) values. Enrichment *P* values were corrected for multiple testing using false discovery rate (FDR) and considered statistically significant if <0.05. Heatmaps were generated using the R package pheatmap v1.0.12 and the R/Bioconductor package ComplexHeatmap[89] v.2.14.0.

Single-cell RNAseq

Cell processing and library preparation. scRNAseq libraries were generated using a microfluidics-based approach on Chromium Controller (10x Genomics) using the Chromium Single Cell 39 Reagent Kit v3.1 according to the manufacturer's instructions. Briefly, single cells from neural mixed cultures were obtained by dissociation with Accutase of duplicate wells per condition. Single cells were obtained from brain spheroids by dissociation with Papain dissociation system (Worthington Biochemical) as previously described[90]. Cells from duplicate wells for mixed cultures or duplicate spheroids were pooled and finally suspended in sterile PBS 0.04% BSA at a concentration of 1,000 cells/μL. 16,000 cells were added to each channel to achieve a recovery rate of 10,000 cells per sample. Cells were partitioned in Gel Beads in Emulsion and lysed, followed by RNA barcoding, RT, and PCR amplification (13 cycles). The concentration of the scRNAseq libraries was determined using Qubit v3.0, and size distribution was assessed using an Agilent 4200 TapeStation system. Libraries were sequenced on an Illumina NovaSeq instrument (paired-end, 150-bp read length).

Data processing and graph-based clustering. Raw data from scRNAseq was analyzed and processed into a transcript count matrix by Cell Ranger v4.0.0 (10x genomics) from the Chromium Single Cell Software Suite by 10x Genomics. Fastq files were generated using the Cell Ranger "mkfastq" command with default parameters. Gene counts for each cell were quantified with the Cell Ranger "count" command with default parameters. For all analyses, the human genome (GRCh38.p13) was used as the reference. The resultant gene expression matrix was imported into the R statistical environment for further analysis. Cell filtering, data normalization, and clustering were carried out using the R package Seurat[91] v3.2.2. For each cell, we calculated the following quality measures: the percentage of mitochondrial genes, the total read count in genes, and the number of expressed genes. Cells with a ratio of mitochondrial vs. endogenous gene expression >0.2 were excluded as putative dying cells. Cells expressing <200 or >6000 total genes were also discarded as putative poorly informative cells and multiplets. Counts were normalized using the Seurat function "NormalizeData" with default parameters. Expression data were then scaled using the "Scale-Data" function, regressing on a number of unique molecular identifiers, percentage of mitochondrial gene expression, and difference between S and G2M scores. Cell cycle scores were calculated using the "CellCycleScoring function".

The different single-cell datasets were integrated in a single object using the R package Harmony v1.0[92] for dealing with experimental and

biological confounding factors and removing batch effects. Dimensionality reduction was then performed with principal component analysis on the batch-corrected data. Uniform Manifold Approximation and Projection (UMAP) dimensionality reduction[93] was performed on the calculated principal components to obtain a 2D representation for data visualization. Cell clusters were identified using the Louvain algorithm at resolution r = 0.6, implemented by the "FindCluster" function of Seurat. To identify cell types within each cluster, a comprehensive manual annotation was performed. A list of marker genes for different cell types was collected from the PanglaoDB database[94] and from a literature-curated set of relevant marker genes[95–99]. Then, it was compared with cluster-specific markers identified by the "FindAllMarkers" function (iteratively comparing one cluster against all the others) from the Seurat package.

Differential expression and GSEA. To find the differentially expressed (marker) genes for the annotated clusters, the "FindMarkers" function (for two condition comparison) from the Seurat package was used with default parameters. Significant differentially expressed genes were identified using the following parameters: adjusted P values < 0.05, average log FC > 0.25, and percentage of cells with expression >0.1. Downstream GSEA analysis was performed with R/Bioconductor package clusterProfiler[88] v3.18 using the Hallmark gene sets from the Molecular Signatures Database (MSigDB). Enriched terms with a q value < 0.05 were considered statistically significant. Heatmaps were generated using the R package pheatmap v1.0.12 and the R/Bioconductor package ComplexHeatmap[89] v.2.14.0. Charts and images were produced using R package ggplot2.

CXCL8 ELISA

Quantification of CXCL8 in astrocyte supernatants was done with Human CXCL8/IL-8 Quantikine ELI-SA Kit (R&D Systems) according to the manufacturer's instructions. Analyses were performed on pooled supernatants from experimental triplicates coming from 3–4 independent experiments at 1:10 dilution. Optical density was measured in an Omega Plate Reader (BMG Labtech) set to 450 nm followed by measurement at 540 nm for background subtraction.

Animals, AAV injections and brain tissue collection

Animal experiments aimed at performing snRNAseq and IF characterization of DNA damage foci and gliosis in the striatum (Figs. 6, 7 and S14) were approved by the Institutional Animal Care and Use Committee (IACUC) of Lampire Biological Laboratories (Protocol No. IAUFSPK#3). All animals were housed on a 12:12 h light–dark cycle. The temperature in housing rooms was 21.5 ± 1.5 °C and relative humidity ranged between 40–70%. Standard chow (Teklad Global 2016) and water were available ad libitum. Striatal snRNAseq experiments were performed on adult (9-week-old) C56BL/6 J male mice sourced from Jackson Labs (Jax Stock 000664). Anesthetized animals (n = 2) received stereotaxic bilateral intraparenchymal (IPa) injections into the striatum with AAV9-CAG-GFP at 1×10^{10} vg in 3 µl/hemisphere (2×10^{10} vg total in 6 µl/mouse brain). This vector dose was chosen as a standard dose used for pre-clinical testing in several settings, independently of toxicity, and because it has been shown to induce glial cell activation and brain infiltration in previous mouse studies using the same route of administration[36,37,100]. Control animals (n = 2) received 3 µl vehicle per hemisphere (6 µl/mouse brain). Vehicle was composed of 180 mM Sodium Chloride, 10 mM Sodium Phosphate, 0.001% Pluronic F68, pH 7.3. Striatal injection coordinates: ML: +/−2.0, AP: 0.5, DV: -3.7. Mice were sacrificed 28 days post-injection. Deeply anesthetized animals were transcardially perfused with ice-cold PBS. Whole brains were removed, and striatum was dissected from both hemispheres. The dissected striatal tissues were flash-frozen in liquid nitrogen and stored in -80 °C until used. Striatal samples from two mice in each group (AAV9 and vehicle) were aggregated for RNA extraction and library preparation. For IF staining of brain striatal sections, adult C56BL/6J male mice received IPa injections of AAV9-CAG-GFP vector (n = 3) as described above at a dose of 1×10^{10} vg in 3 µl per hemisphere (6 µl/mouse brain). Control animals (n = 2) received 3 µl vehicle per hemisphere (6 µl/mouse brain). 28 days post-injection, deeply anesthetized mice were transcardially perfused with ice-cold PBS, followed with 4% PFA in PBS, after which brains were dissected and processed for FFPE.

Experiments aimed at studying the immunomodulatory effect of cGAS, STING and p53 inhibitors were conducted at Charles River Finland as specified in the license authorized by the national Animal Experiment Board of Finland and according to the National Institutes of Health (Bethesda, MD, USA) guidelines for the care and use of laboratory animals. Studies were conducted in accordance with the Guide for the Care and Use of Laboratory Animals (National Research Council 2011) and European Union directive 2010/63 under [ESAVI/8072/2021] approved by the national Project Authorization Board. The experiments were approved by the site's Animal Welfare Team. Experiments were performed in adult C56BL/6J male mice (Charles River Laboratoires, 7-weeks old) receiving bilateral injections into the striatum of AAV vector or diluent as indicated in the figure legend in Fig. S20. In addition, indicated groups received concomitant daily intraperitoneal (I.P.) injections of vehicle (for vehicle and AAV groups), or the cGAS inhibitor RU.521 (cGASi, 10 mg/kg), the p53 inhibitor Pifithrin-α (p53i, 2.5 mg/kg), or every three-day injection of H151 (STINGi, 10 mg/kg).

Single-nucleus RNAseq

Two mice from each treatment group (AAV9 and vehicle) were processed for these experiments. Both striata from each mouse were pooled prior to nuclear isolation. Nuclei were isolated using the 10x Genomics Nuclei Isolation Kit with RNase Inhibitor (10x Genomics) with minor modifications. First, flash-frozen tissue was transferred to ice-cold lysis buffer (from the Nuclei Isolation Kit) in a 1 mL glass tissue homogenizer (Wheaton). After douncing, the tissue lysate was resuspended and left to incubate for 10 min on ice. Additional steps followed the manufacturer's instructions. During the first wash (after debris removal), the nuclear suspension was incubated with rotation for 20 min at 4 °C with DAPI staining solution (Abcam) at a final concentration of 5 µM. Following a spin and final resuspension, nuclei with 2 N DNA content were purified by fluorescence-activated nuclear sorting (Sony Cell Sorter) based on DAPI-fluorescence and collected in Wash and Resuspension Buffer (PBS, 0.5% BSA, and 0.2U/µl RNase Inhibitor - prepared according to kit instructions). Sorted 2 N nuclei event count and final volume was used to inform sample loading volume, and the nuclei were immediately loaded onto 10x Chromium Single Cell 3' Kit v3.1 chips at ~20k nuclei per sample (this loading concentration was optimized based on sorter nuclear count and 10x nuclear recovery). Libraries were generated following the manufacturer's protocol and were sequenced using the Illumina NextSeq 2000.

Data processing and graph-based clustering

Raw data from snRNAseq was analyzed and processed into transcript count matrix by Cell Ranger (https://www.10xgenomics.com/support/software/cell-ranger, v7.0.0) from the Chromium Single Cell Software Suite by 10x Genomics. Fastq files were generated using the Cell Ranger mkfastq command with default parameters. Gene counts for each cell were quantified with the Cell Ranger count command with default parameters. For all analyses, the mouse genome (GRCm38, release 93) plus the AAV9 genome was used as a reference. The resultant gene expression matrix was imported into the R statistical environment for further analysis. Cell filtering, data normalization, and clustering were carried out using the R package Seurat[91] v4.9.9.9060. For each cell, the following quality measures were calculated:

percentage of mitochondrial genes and number of total genes expressed. Cells with a ratio of mitochondrial vs. endogenous gene expression >5% were excluded as putative dying cells. Cells expressing <200 or >5000 total genes were also discarded as putative poorly informative cells and multiplets. The different single-nucleus datasets were integrated in a single object using the sctransform v2.0 approach[101] for dealing with experimental and biological confounding factors and removing batch effects. Dimensionality reduction was then performed with principal component analysis on the batch-corrected data. Uniform Manifold Approximation and Projection (UMAP) dimensionality reduction[93] was performed on the calculated principal components to obtain a 2D representation for data visualization. Cell clusters were identified using the Louvain algorithm at resolution $r = 0.1$, implemented by the FindCluster function of Seurat. To characterize each cluster, a comprehensive manual annotation was performed. A list of marker genes for different cell types was collected from a literature-curated set of relevant marker genes[102,103].

Differential expression and GSEA. To find the differentially expressed (marker) genes for the annotated clusters, the functions FindConservedMarkers (iteratively comparing one cluster against all the others) from the Seurat package was used with default parameters. Cells with EGFP expression levels passing a certain threshold, determined by non-cellular barcodes and immunohistochemical signals, were kept for downstream analysis. Downstream analysis, including GSEA, was performed with R/Bioconductor package fgsea using two databases in the Molecular Signatures Database, Kyoto Encyclopaedia of Genes and Genomes and Hallmark gene sets. Significance testing was performed with the fgsea package in Bioconductor, which uses a permutation-based approach, where gene set enrichment scores are compared to a null distribution of random permutations of the gene rankings. The *p*-value represents a proportion of random permutations with enrichment scores more extreme than the given gene set, adjusted using the Benjamini-Hochberg correction to control the false discovery rate. Enriched terms with a q value < 0.05 were considered statistically significant. Charts and images were produced using the R package ggplot2.

Clustering of single-cell and single-nuclei RNAseq data

For the generation of Supplementary Fig. 13, raw counts from the human scRNAseq datasets (2D mixed neural-glial cultures and 3D spheroids) and the mouse snRNAseq dataset were normalized. Individual-cell-type-level normalized gene expression profile averages were calculated, and a gene set variation analysis (GSVA) was performed by calculation of pathway activity scores against the Hallmark gene set collection from the Molecular Signatures Database (MSigDB) using the GSVA implementation from the R/Bioconductor package GSVA (version 1.46.0)[104]. In brief, GSVA estimates a normalized relative expression level per gene across samples, which is then rank-ordered for each sample and aggregated into gene sets by calculating sample-wise enrichment scores using a Kolmogorov–Smirnov-like rank statistic. The following parameters were used to evaluate the GSVA function: mx.diff=TRUE, kcdf=c("Gaussian"), min.sz = 5, max.sz = 500. The resulting enrichment scores were used for clustering the samples in a pathway-centric manner by k-means clustering using the R/Bioconductor package ComplexHeatmap[89].

Statistics

Data are reported as mean, mean ± SD or mean ± SEM as indicated in the figure legends. GraphPad Prism 10 (GraphPad Software) was used for statistical analyses. $P < 0.05$ was considered significant. For all the data sets, statistical analyses were performed using one-way ANOVA with Tukey's or Bonferroni's post-hoc correction as indicated. The statistical analysis performed for each data set is indicated in the corresponding figure legend. For all figures, $^{*}P < 0.05$, $^{**}P < 0.01$, $^{***}P < 0.001$.

Reporting summary

Further information on research design is available in the Nature Portfolio Reporting Summary linked to this article.

Data availability

All relevant data are included in the manuscript. Bulk and single-cell RNA-seq data have been deposited in the GEO database in a SuperSeries with the accession code GSE253824 under public access (https://www.ncbi.nlm.nih.gov/geo/query/acc.cgi?acc=GSE253824). Single-nuclei RNA-seq data has been deposited with the accession code GSE256350 under public access (https://www.ncbi.nlm.nih.gov/geo/query/acc.cgi?acc=GSE256350). Accession numbers are listed in the Supplementary Table 2. Source data are provided with this paper.

Code availability

All original code has been deposited at Gitlab under public access under public access (http://www.bioinfotiget.it/gitlab/custom/costaverdera_natcom2025).

References

1. Costa-Verdera, H. et al. Understanding and tackling immune responses to adeno-associated viral vectors. *Hum. Gene Ther.* **34**, 836–852 (2023).
2. Costa Verdera, H., Kuranda, K. & Mingozzi, F. AAV vector immunogenicity in humans: a long journey to successful gene transfer. *Mol. Ther.* **28**, 723–746 (2020).
3. Perez, B. A., Shutterly, A., Chan, Y. K., Byrne, B. J. & Corti, M. Management of neuroinflammatory responses to AAV-mediated gene therapies for neurodegenerative diseases. *Brain Sci.* **10**, 119 (2020).
4. High-dose AAV gene therapy deaths. *Nat. Biotechnol.* **38**, 910–910 (2020).
5. Lek, A. et al. Death after high-dose rAAV9 gene therapy in a patient with Duchenne's muscular dystrophy. *N. Engl. J. Med.* **389**, 1203–1210 (2023).
6. Kang, L. et al. AAV vectors applied to the treatment of CNS disorders: Clinical status and challenges. *J. Control. Rel.* **355**, 458–473 (2023).
7. Keiser, M. S. et al. Toxicity after AAV delivery of RNAi expression constructs into nonhuman primate brain. *Nat. Med.* **27**, 1982–1989 (2021).
8. Golebiowski, D. et al. Direct intracranial injection of AAVrh8 encoding monkey β-N-Acetylhexosaminidase causes neurotoxicity in the primate brain. *Hum. Gene Ther.* **28**, 510–522 (2017).
9. Rosenberg, J. B. et al. Safety of direct Intraparenchymal AAVrh.10-mediated central nervous system gene therapy for metachromatic leukodystrophy. *Hum. Gene Ther.* **32**, 563–580 (2021).
10. Zerah, M. et al. Intracerebral gene therapy using AAVrh.10-hARSA recombinant vector to treat patients with early-onset forms of metachromatic leukodystrophy: preclinical feasibility and safety assessments in nonhuman primates. *Hum. Gene Ther. Clin. Dev.* **26**, 113–124 (2015).
11. Golebiowski, D. et al. Direct intracranial injection of AAVrh8 encoding monkey beta-N-Acetylhexosaminidase causes neurotoxicity in the primate brain. *Hum. Gene Ther.* **28**, 510–522 (2017).
12. Mueller, C. et al. SOD1 suppression with adeno-associated virus and MicroRNA in familial ALS. *N. Engl. J. Med.* **383**, 151–158 (2020).
13. Bharucha-Goebel, D. X. et al. Intrathecal gene therapy for giant axonal neuropathy. *N. Engl. J. Med.* **390**, 1092–1104 (2024).
14. Hinderer, C. et al. Severe toxicity in nonhuman primates and piglets following high-dose intravenous administration of an adeno-associated virus vector expressing human SMN. *Hum. Gene Ther.* **29**, 285–298 (2018).
15. Hordeaux, J. et al. Adeno-associated virus-induced dorsal root ganglion pathology. *Hum. Gene Ther.* **31**, 808–818 (2020).

16. Sondhi, D. et al. Slowing late infantile Batten disease by direct brain parenchymal administration of a rh.10 adeno-associated virus expressing CLN2. *Sci. Transl. Med.* **12**, eabb5413 (2020).
17. Colella, P., Ronzitti, G. & Mingozzi, F. Emerging issues in AAV-mediated in vivo gene therapy. *Mol. Ther. Methods Clin. Dev.* **8**, 87–104 (2017).
18. Kuranda, K. et al. Exposure to wild-type AAV drives distinct capsid immunity profiles in humans. *J. Clin. Invest* **128**, 5267–5279 (2018).
19. Konkle, B. A. et al. BAX 335 hemophilia B gene therapy clinical trial results: potential impact of CpG sequences on gene expression. *Blood* **137**, 763–774 (2021).
20. Rogers, G. L. et al. Plasmacytoid and conventional dendritic cells cooperate in crosspriming AAV capsid-specific CD8(+) T cells. *Blood* **129**, 3184–3195 (2017).
21. Kumar, S. R. P. et al. TLR9-independent CD8+ T cell responses in hepatic AAV gene transfer through IL-1R1-MyD88 signaling. *Mol. Ther.* **32**, 325–339 (2024).
22. Zhu, J., Huang, X. & Yang, Y. The TLR9-MyD88 pathway is critical for adaptive immune responses to adeno-associated virus gene therapy vectors in mice. *J. Clin. Invest* **119**, 2388–2398 (2009).
23. Smith, C. J. et al. Pre-existing humoral immunity and complement pathway contribute to immunogenicity of adeno-associated virus (AAV) vector in human blood. *Front Immunol.* **13**, 999021 (2022).
24. West, C. et al. Complement activation by AAV-neutralizing antibody complexes. *Hum. Gene Ther.* **34**, 554–566 (2023).
25. Zaiss, A. K. et al. Complement is an essential component of the immune response to adeno-associated virus vectors. *J. Virol.* **82**, 2727–2740 (2008).
26. Piras, F. et al. Lentiviral vectors escape innate sensing but trigger p53 in human hematopoietic stem and progenitor cells. *EMBO Mol. Med.* **9**, 1198–1211 (2017).
27. Piras, F. & Kajaste-Rudnitski, A. Antiviral immunity and nucleic acid sensing in haematopoietic stem cell gene engineering. *Gene Ther.* **28**, 16–28 (2021).
28. Hirsch, M. L. et al. Viral single-strand DNA induces p53-dependent apoptosis in human embryonic stem cells. *PLoS One* **6**, e27520 (2011).
29. Cho, H. et al. Differential innate immune response programs in neuronal subtypes determine susceptibility to infection in the brain by positive-stranded RNA viruses. *Nat. Med.* **19**, 458–464 (2013).
30. Hung, Y. F. et al. Endosomal TLR3, TLR7, and TLR8 control neuronal morphology through different transcriptional programs. *J. Cell Biol.* **217**, 2727–2742 (2018).
31. Vercauteren, K. et al. Superior in vivo transduction of human hepatocytes using engineered AAV3 Capsid. *Mol. Ther.* **24**, 1042–1049 (2016).
32. Hordeaux, J. et al. The neurotropic properties of AAV-PHP.B are limited to C57BL/6J mice. *Mol. Ther.* **26**, 664–668 (2018).
33. Mingozzi, F. et al. Overcoming preexisting humoral immunity to AAV using capsid decoys. *Sci. Transl. Med* **5**, 194ra192 (2013).
34. Marton, R. M. et al. Differentiation and maturation of oligodendrocytes in human three-dimensional neural cultures. *Nat. Neurosci.* **22**, 484–491 (2019).
35. Mason, M. R. et al. Comparison of AAV serotypes for gene delivery to dorsal root ganglion neurons. *Mol. Ther.* **18**, 715–724 (2010).
36. Hollidge, B. S. et al. Kinetics and durability of transgene expression after intrastriatal injection of AAV9 vectors. *Front. Neurol.* **13**, 1051559 (2022).
37. Guo, Y. et al. High-titer AAV disrupts cerebrovascular integrity and induces lymphocyte infiltration in adult mouse brain. *Mol. Ther. Methods Clin. Dev.* **31**, 101102 (2023).
38. Hordeaux, J. et al. MicroRNA-mediated inhibition of transgene expression reduces dorsal root ganglion toxicity by AAV vectors in primates. *Sci. Transl. Med.* **12**, eaba9188 (2020).
39. Sun, W. et al. SOX9 Is an Astrocyte-specific nuclear marker in the adult brain outside the neurogenic regions. *J. Neurosci.* **37**, 4493–4507 (2017).
40. Ge, M. M. et al. Galectin-3 in microglia-mediated neuroinflammation: implications for central nervous system diseases. *Curr. Neuropharmacol.* **20**, 2066–2080 (2022).
41. Pollock, N. M. et al. Gasdermin D activation in oligodendrocytes and microglia drives inflammatory demyelination in progressive multiple sclerosis. *Brain Behav. Immun.* **115**, 374–393 (2024).
42. Bertolini, T. B. et al. Effect of CpG depletion of vector genome on CD8(+) T cell responses in AAV gene therapy. *Front. Immunol.* **12**, 672449 (2021).
43. Wright, J. F. Quantification of CpG Motifs in rAAV genomes: avoiding the toll. *Mol. Ther.* **28**, 1756–1758 (2020).
44. Chan, Y. K. et al. Engineering adeno-associated viral vectors to evade innate immune and inflammatory responses. *Sci. Transl. Med.* **13**, eabd3438 (2021).
45. Martino, A. T. et al. The genome of self-complementary adeno-associated viral vectors increases Toll-like receptor 9-dependent innate immune responses in the liver. *Blood* **117**, 6459–6468 (2011).
46. Wu, T. et al. Self-complementary AAVs induce more potent transgene product-specific immune responses compared to a single-stranded genome. *Mol. Ther.* **20**, 572–579 (2012).
47. Shao, W. et al. Double-stranded RNA innate immune response activation from long-term adeno-associated virus vector transduction. *JCI Insight* **3**, e120474 (2018).
48. Salabarria, S. M. et al. Thrombotic microangiopathy following systemic AAV administration is dependent on anti-capsid antibodies. *J. Clin. Invest.* **134**, e173510 (2024).
49. Balakrishnan, B. et al. Activation of the cellular unfolded protein response by recombinant adeno-associated virus vectors. *PLoS One* **8**, e53845 (2013).
50. Au, H. K. E., Isalan, M. & Mielcarek, M. Gene therapy advances: a meta-analysis of AAV usage in clinical settings. *Front Med.* **8**, 809118 (2021).
51. Nathwani, A. C., McIntosh, J. & Sheridan, R. Liver gene therapy. *Hum. Gene Ther.* **33**, 879–888 (2022).
52. Keam, S. J. Eladocagene Exuparvovec: First approval. *Drugs* **82**, 1427–1432 (2022).
53. Kishimoto, T. K. & Samulski, R. J. Addressing high dose AAV toxicity - 'one and done' or 'slower and lower'? *Expert Opin. Biol. Ther.* **22**, 1067–1071 (2022).
54. Klein, R. S. & Hunter, C. A. Protective and pathological immunity during central nervous system infections. *Immunity* **46**, 891–909 (2017).
55. Ising, C. & Heneka, M. T. Functional and structural damage of neurons by innate immune mechanisms during neurodegeneration. *Cell Death Dis.* **9**, 120 (2018).
56. Hosel, M. et al. Toll-like receptor 2-mediated innate immune response in human nonparenchymal liver cells toward adeno-associated viral vectors. *Hepatology* **55**, 287–297 (2012).
57. Schwartz, R. A. et al. The Mre11/Rad50/Nbs1 complex limits adeno-associated virus transduction and replication. *J. Virol.* **81**, 12936–12945 (2007).
58. Pezone, A. et al. Inflammation and DNA damage: cause, effect or both. *Nat. Rev. Rheumatol.* **19**, 200–211 (2023).
59. Ning, K. et al. Adeno-associated virus monoinfection induces a DNA damage response and DNA repair that contributes to viral DNA replication. *mBio* **14**, e0352822 (2023).
60. Schwartz, R. A., Carson, C. T., Schuberth, C. & Weitzman, M. D. Adeno-associated virus replication induces a DNA damage response coordinated by DNA-dependent protein kinase. *J. Virol.* **83**, 6269–6278 (2009).

61. Cervelli, T. et al. Processing of recombinant AAV genomes occurs in specific nuclear structures that overlap with foci of DNA-damage-response proteins. *J. cell Sci.* **121**, 349–357 (2008).
62. Leroy, B. et al. Analysis of TP53 mutation status in human cancer cell lines: a reassessment. *Hum. Mutat.* **35**, 756–765 (2014).
63. Mitchell, J. et al. Hepatitis C virus indirectly disrupts DNA damage-induced p53 responses by activating Protein Kinase R. *mBio* **8**, e00121–00117 (2017).
64. Herzog, R. W. Immune responses to AAV Capsid: Are mice not humans after all? *Mol. Ther.* **15**, 649–650 (2007).
65. Tahtinen, S. et al. IL-1 and IL-1ra are key regulators of the inflammatory response to RNA vaccines. *Nat. Immunol.* **23**, 532–542 (2022).
66. Giordano, A. M. S. et al. DNA damage contributes to neurotoxic inflammation in Aicardi-Goutieres syndrome astrocytes. *J. Exp. Med.* **219**, e20211121 (2022).
67. Reinert, L. S. et al. Brain immune cells undergo cGAS/STING-dependent apoptosis during herpes simplex virus type 1 infection to limit type I IFN production. *J. Clin. Invest.* **131**, e136824 (2021).
68. Novak, J. et al. Interleukin-1α associates with the tumor suppressor p53 following DNA damage. *Sci. Rep.* **10**, 6995 (2020).
69. Ubertini, V. et al. Mutant p53 gains new function in promoting inflammatory signals by repression of the secreted interleukin-1 receptor antagonist. *Oncogene* **34**, 2493–2504 (2015).
70. Ghosh, M., Saha, S., Li, J., Montrose, D. C. & Martinez, L. A. p53 engages the cGAS/STING cytosolic DNA sensing pathway for tumor suppression. *Mol. Cell* **83**, 266–280.e266 (2023).
71. Gulen, M. F. et al. cGAS–STING drives ageing-related inflammation and neurodegeneration. *Nature* **620**, 374–380 (2023).
72. Sanchez, G. A. M. et al. JAK1/2 inhibition with baricitinib in the treatment of autoinflammatory interferonopathies. *J. Clin. Investig.* **128**, 3041–3052 (2018).
73. Balci, S., Ekinci, R. M. K., de Jesus, A. A., Goldbach-Mansky, R. & Yilmaz, M. Baricitinib experience on STING-associated vasculopathy with onset in infancy: A representative case from Turkey. *Clin. Immunol.* **212**, 108273 (2020).
74. Volpi, S. et al. Efficacy and adverse events during Janus Kinase inhibitor treatment of SAVI Syndrome. *J. Clin. Immunol.* **39**, 476–485 (2019).
75. Gougeon, M. L. et al. Cell-mediated immunity to NAGLU Transgene following intracerebral gene therapy in children with Mucopolysaccharidosis Type IIIB Syndrome. *Front Immunol.* **12**, 655478 (2021).
76. Meneghini, V. et al. Generation of human induced pluripotent stem cell-derived bona fide neural stem cells for ex vivo gene therapy of metachromatic leukodystrophy. *Stem Cells Transl. Med.* **6**, 352–368 (2017).
77. Mangiameli, E. et al. Human iPSC-based neurodevelopmental models of globoid cell leukodystrophy uncover patient- and cell type-specific disease phenotypes. *Stem Cell Rep.* **16**, 1478–1495 (2021).
78. Frati, G. et al. Human iPSC-based models highlight defective glial and neuronal differentiation from neural progenitor cells in metachromatic leukodystrophy. *Cell Death Dis.* **9**, 698 (2018).
79. Chambers, S. M. et al. Highly efficient neural conversion of human ES and iPS cells by dual inhibition of SMAD signaling. *Nat. Biotechnol.* **27**, 275–280 (2009).
80. Giordano, A. M. S., Abou Alezz, M., Merelli, I. & Kajaste-Rudnitski, A. Protocol to differentiate monolayer human induced pluripotent stem cells into inflammatory responsive astrocytes. *STAR Protoc.* **4**, 102142 (2023).
81. Santos, R. et al. Differentiation of inflammation-responsive astrocytes from glial progenitors generated from human induced pluripotent stem cells. *Stem Cell Rep.* **8**, 1757–1769 (2017).
82. Mangiameli, E., Freschi, M., Luciani, M. & Gritti, A. Generation of neuronal/glial mixed cultures from human induced pluripotent stem cells (hiPSCs). *Methods Cell Biol.* **171**, 229–245 (2022).
83. Collaud, F. et al. Preclinical development of an AAV8-hUGT1A1 vector for the treatment of Crigler-Najjar Syndrome. *Mol. Ther. Methods Clin. Dev.* **12**, 157–174 (2019).
84. Montini, E. et al. Hematopoietic stem cell gene transfer in a tumor-prone mouse model uncovers low genotoxicity of lentiviral vector integration. *Nat. Biotechnol.* **24**, 687–696 (2006).
85. Lock, M. et al. Characterization of a recombinant adeno-associated virus type 2 Reference Standard Material. *Hum. Gene Ther.* **21**, 1273–1285 (2010).
86. Dobin, A. et al. STAR: ultrafast universal RNA-seq aligner. *Bioinformatics* **29**, 15–21 (2013).
87. Liao, Y., Smyth, G. K. & Shi, W. featureCounts: an efficient general purpose program for assigning sequence reads to genomic features. *Bioinformatics* **30**, 923–930 (2014).
88. Yu, G., Wang, L.-G., Han, Y. & He, Q.-Y. clusterProfiler: an R package for comparing biological themes among gene clusters. *OMICS: A J. Integr. Biol.* **16**, 284–287 (2012).
89. Gu, Z., Eils, R. & Schlesner, M. Complex heatmaps reveal patterns and correlations in multidimensional genomic data. *Bioinformatics* **32**, 2847–2849 (2016).
90. Yoon, S. J. et al. Reliability of human cortical organoid generation. *Nat. Methods* **16**, 75–78 (2019).
91. Stuart, T. et al. Comprehensive integration of single-cell data. *Cell* **177**, 1888–1902.e1821 (2019).
92. Korsunsky, I. et al. Fast, sensitive and accurate integration of single-cell data with Harmony. *Nat. Methods* **16**, 1289–1296 (2019).
93. Becht, E. et al. Dimensionality reduction for visualizing single-cell data using UMAP. *Nat. Biotechnol.* **37**, 38–44 (2018).
94. Franzén, O., Gan, L. M. & Björkegren, J. L. M. PanglaoDB: a web server for exploration of mouse and human single-cell RNA sequencing data. *Database* **2019**, baz046 (2019).
95. Darmanis, S. et al. A survey of human brain transcriptome diversity at the single cell level. *Proc. Natl Acad. Sci. USA* **112**, 7285–7290 (2015).
96. Guttikonda, S. R. et al. Fully defined human pluripotent stem cell-derived microglia and tri-culture system model C3 production in Alzheimer's disease. *Nat. Neurosci.* **24**, 343–354 (2021).
97. Jerber, J. et al. Population-scale single-cell RNA-seq profiling across dopaminergic neuron differentiation. *Nat. Genet* **53**, 304–312 (2021).
98. Tanaka, Y., Cakir, B., Xiang, Y., Sullivan, G. J. & Park, I. H. Synthetic analyses of single-cell transcriptomes from multiple brain organoids and fetal brain. *Cell Rep.* **30**, 1682–1689.e1683 (2020).
99. Zhang, Y. et al. Purification and characterization of progenitor and mature human astrocytes reveals transcriptional and functional differences with mouse. *Neuron* **89**, 37–53 (2016).
100. Ortinski, P. I. et al. Selective induction of astrocytic gliosis generates deficits in neuronal inhibition. *Nat. Neurosci.* **13**, 584–591 (2010).
101. Choudhary, S. & Satija, R. Comparison and evaluation of statistical error models for scRNA-seq. *Genome Biol.* **23**, 27 (2022).
102. Malaiya, S. et al. Single-nucleus RNA-Seq reveals dysregulation of striatal cell identity due to Huntington's disease mutations. *J. Neurosci.* **41**, 5534–5552 (2021).
103. Xia, E. An Analysis of Cellular Identities in the Murine Striatum Using Single Nuclei RNA-Sequencing. (Icahn School of Medicine ProQuest Dissertations & Theses, 28265299, 2020). https://www.proquest.com/openview/40a956a1482e9d2603c367b5ab4ea71b/1?cbl=18750&diss=y&pq-origsite=gscholar.
104. Hanzelmann, S., Castelo, R. & Guinney, J. GSVA: gene set variation analysis for microarray and RNA-seq data. *BMC Bioinforma.* **14**, 7 (2013).

Acknowledgements
This work was supported by grants from the European Research Council (ERC-CoG 819815-ImmunoStem), Fondazione Telethon (TTAGD0222T to AG), the FNIH (2022-BGTC003), and a Sponsored Research Agreement with Spark Therapeutics to AKR. Results shown in Fig. 6B, C and E were performed as a part of the ARDAT project. The ARDAT project has received funding from the Innovative Medicines Initiative 2 Joint Undertaking under grant agreement No 945473. This Joint Undertaking receives support from the European Union's Horizon 2020 research and innovation programme and EFPIA. This communication reflects the views of the authors, and neither the IMI nor the European Union, EFPIA or any other partners are liable for any use that may be made of the information contained herein. GC conducted this study as partial fulfilment of his Ph.D. in Molecular Medicine, Programme in Gene and Cell Therapy, International Ph.D. School, Vita-Salute San Raffaele University, Milan, Italy. We wish to thank Julie Tahraoui and Maria Sole Giordano for initial help and suggestions for hiPSC differentiation, staining and image acquisition, Pietro Pola for initial help in the setup of the 3D spheroid protocol, Cesare Covino from Alembic and Yu-Chen Hwang from the bioimaging platform at Spark Therapeutics for the help with immunofluorescence imaging acquisition and analysis. The authors thank Eric Kostuk, Karthik Ramanathan, Brittany Wicks, Robert Straub, and Tiffany Smith from In Vivo Neuro Group at Spark Therapeutics, Inc. for animal study assistance. This study was partially funded by Spark Therapeutics. G.R. has received funding from the Innovative Medicines Initiative 2 Joint Undertaking (JU) under grant agreement No 945473. The remaining authors declare no competing interests.

Author contributions
H.C.V. designed and performed experiments, analysed data and wrote the manuscript. V.M., E.M., Z.F., A.A., E.F., Y.D. and E.E. contributed to the experimental design and execution. E.V., I.C., R.C., G.C. and B.B. contributed to vector design, vector production, and setup of drug concentrations. A.G., G.R., F.M. and K.K. designed and supervised experiments. M.A.A., I.M. and X.H. analysed NGS data. Y.K.C. and S.P. contributed to revisions with reagents and experiments, respectively. AKR designed and supervised experiments and wrote the manuscript.

Competing interests
The authors declare no competing interests.

Additional information
Supplementary information The online version contains supplementary material available at https://doi.org/10.1038/s41467-025-58778-3.

Correspondence and requests for materials should be addressed to Anna Kajaste-Rudnitski.

Peer review information *Nature Communications* thanks Daniel Stone and the other, anonymous, reviewers for their contribution to the peer review of this work. A peer review file is available.